OPTICAL PROPERTIES OF CdS AND CdTe MICROCRYSTALLITES IN GLASS AND AN OPTICAL ASSOCIATIVE MEMORY

by

Victor Clark Esch

A Dissertation Submitted to the Faculty of the

COMMITTEE ON OPTICAL SCIENCES (GRADUATE)

In Partial Fulfillment of the Requirements
For the Degree of

DOCTOR OF PHILOSOPHY

In the Graduate College of

THE UNIVERSITY OF ARIZONA

1 9 9 0

Order Number 9022104

Optical properties of CdS and CdTe microcrystallites in glass and an optical associative memory

Esch, Victor Clark, Ph.D.

The University of Arizona, 1990

U·M·I
300 N. Zeeb Rd.
Ann Arbor, MI 48106

OPTICAL PROPERTIES OF CdS AND CdTe MICROCRYSTALLITES IN GLASS AND AN OPTICAL ASSOCIATIVE MEMORY

by

Victor Clark Esch

A Dissertation Submitted to the Faculty of the

COMMITTEE ON OPTICAL SCIENCES (GRADUATE)

In Partial Fulfillment of the Requirements
For the Degree of

DOCTOR OF PHILOSOPHY

In the Graduate College of

THE UNIVERSITY OF ARIZONA

1 9 9 0

THE UNIVERSITY OF ARIZONA
GRADUATE COLLEGE

As members of the Final Examination Committee, we certify that we have read the dissertation prepared by Victor Clark Esch

entitled Optical Properties of CdS and CdTe Microcrystallites in Glass and An Optical Associative Memory

and recommend that it be accepted as fulfilling the dissertation requirement for the Degree of Doctor of Philosophy.

Hyatt M. Gibbs, Dissertation Director	February 23, 1990 Date
Nasser Peyghambarian	February 23, 1990 Date
Galina Khitrova	February 23, 1990 Date
	Date
	Date

Final approval and acceptance of this dissertation is contingent upon the candidate's submission of the final copy of the dissertation to the Graduate College.

I hereby certify that I have read this dissertation prepared under my direction and recommend that it be accepted as fulfilling the dissertation requirement.

Hyatt M. Gibbs Dissertation Director	3-6-90 Date

STATEMENT BY AUTHOR

This dissertation has been submitted in partial fulfillment of requirements for an advanced degree at The University of Arizona and is deposited in the University Library to be made available to borrowers under rules of the Library.

Brief quotations from this dissertation are allowable without special permission, provided that accurate acknowledgment of source is made. Requests for permission for extended quotation from or reproduction of the manuscript in whole or in part may be granted by the head of the major department or the Dean of the Graduate College when in his or her judgement the proposed use of the material is in the interests of scholarship. In all other instances, however, permission must be obtained from the author.

SIGNED: 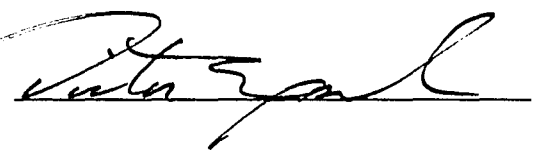

Dedicated to my family,

and especially my grandparents.

ACKNOWLEDGEMENTS

I would like to thank my advisor Professor Hyatt Gibbs for the opportunities that he has given me, particularly the experience of working with him. My most effective learning was done watching him at work. I would also like to thank Galina Khitrova for her generous and light hearted help, and also her considerable contributions to this dissertation. Her technical guidance, particularly with subjects that were plainly beyond my comprehension, is particularly appreciated. Thanks also to Professor Nasser Peyghambarian for his help and incisive discussions.

The number of friends and colleagues that have helped me with my work would make a considerable list. Without their help I could have never come close to completing my degree. Those people that I worked with day in and day out, Arturo Chavez-Pirson, Mial Warren, Lon Wang, Rick Feinleib, Russell Pon, Ruxiang Jin, Koo Kang, Brian McGinnis, and Chih-Li Chuang, all deserve particular thanks.

TABLE OF CONTENTS

LIST OF ILLUSTRATIONS

LIST OF TABLES

ABSTRACT

The linear and nonlinear properties of CdTe and CdS microcrystallites, or 'quantum dots', grown in glass were investigated. The CdTe quantum dots investigated, the first ever grown, demonstrated the most confinement peaks observed for quantum dots of this kind. The linear absorption for CdTe was modeled. The growth of the microcrystallites in glass was optimized using quantum confined behavior as the criteria. The temperature dependent red shift of the band gap, and the phonon broadening of the 1s-1s transition feature were measured. The fluorescence spectra for CdS and CdTe were taken and found to be different in some respects.

The quantum confined Franz-Keldysh effect was modeled and measured for CdTe. Very good agreement with theory was found. The effect of trap state electric fields was considered. The Franz-Keldysh effect for bulk-like microcrystallites was observed. The results for CdS quantum dots were not similar to that of CdTe.

The differential absorption for CdS and CdTe was measured with nanosecond time scale optical excitation. Typical differential signals were observed, and long lifetimes were measured. Microsecond time scale excitation was used for CdTe and exceptionally long lifetimes were seen. Differential signals were found to correlate to fluorescence lifetimes. The differential signals were attributed to trap state electric fields (coulombic interaction) with at least two lifetime components. Photodarkening was considered in the context of this trap state scheme.

CHAPTER I

QUANTUM MECHANICAL TREATMENT OF QUANTUM DOT ABSORPTION

The absorption of zero dimensional microcrystallites, or quantum dots, may be treated with elementary quantum mechanics [Miller et al. (1988)]. The electron and hole are simply particles in a box. Complications do arise when the semiconductor material properties such as energy dependent mass of the carriers, and homogeneous and inhomogeneous linewidths, are included. Nevertheless, the following derivation, remedial for some, has been applied to achieve good agreement with experimental measurements.

Two different situations will be treated with the time independent Schrodinger equation. In the case of an unperturbed quantum confined microcrystallite the wave equation is readily solved, and the energy levels for finite and infinite confining potentials can be examined [Schiff (1955)]. With an applied electric field present the radial and θ terms in the equation are coupled, and the infinite well solution is found using the no-electric-field eigenvectors as a basis set. Absorption, with and without an applied electric field, is found.

A short section on crystallite growth is also presented, mainly to acquaint the reader with the mechanism of growth. Good agreement with theory has, however, not been observed.

The time independent Schrodinger equation with an electric field F present is

$$\left[\frac{-\hbar^2}{2m}\nabla^2 + V(r)\right]\psi(r) = E\psi(r) \tag{1.1}$$

and in spherical coordinates

$$\frac{-\hbar^2}{2m_0}\left[\frac{1}{r^2}\frac{\partial}{\partial r}\left(r^2\frac{\partial}{\partial r}\right) + \frac{1}{r^2}\frac{1}{\sin\theta}\frac{\partial}{\partial\theta}\left(\sin\theta\frac{\partial}{\partial\theta}\right) + \frac{1}{r^2\sin^2\theta}\frac{\partial^2}{\partial\phi^2}\right]\psi \tag{1.2}$$
$$+ V(r)\psi - (Fr\cos\theta)\psi = E\psi$$

where V(r) is a sperically symmetric confining potential. Because the electric field couples r and θ, only the ϕ coordinate may be separated. Using $\psi=\chi(r,\theta)\Phi(\phi)$, and $H=\hbar^2/2m_0$,

$$\frac{H}{r^2}\left[\frac{1}{\chi}\frac{\partial}{\partial r}\left(r^2\frac{\partial}{\partial r}\right)\chi + \frac{1}{\chi}\frac{1}{\sin\theta}\frac{\partial}{\partial\theta}\left(\sin\theta\frac{\partial}{\partial\theta}\right)\chi\right] \tag{1.3}$$
$$+ E + Fr\cos\theta - V(r) = -\frac{H}{r^2}\frac{1}{\Phi}\frac{1}{\sin^2\theta}\frac{\partial^2}{\partial\psi^2}\Phi$$

The two sides of this equation are equal and independent so they may each be set equal to a separation constant $-\nu$. The Φ equation

$$\frac{1}{\Phi}\frac{\partial^2\Phi}{\partial\psi^2} = -\nu \tag{1.4}$$

is trivially solved to yield $\nu=m^2$, and the χ equation is written

$$\frac{H}{r^2}\left[\frac{\partial}{\partial r}\left(r^2\,\frac{\partial}{\partial r}\right)+\frac{\partial}{\partial \zeta}(1-\zeta^2)\,\frac{\partial}{\partial \zeta}\right]\chi+\left[Fr\zeta-V(r)-\frac{h}{r^2}\,\frac{m^2}{(1-\zeta^2)}\right]\chi=E\chi \qquad (1.5)$$

having used $\cos\theta=\zeta$. If there is no electric field present this equation may be further separated using $\chi=R(r)\Theta(\theta)=R(r)P(\zeta)$. Using λ as the seperation constant the independent equations are

$$\frac{1}{r^2}\,\frac{\partial}{\partial r}\left(r^2\,\frac{dR}{dr}\right)+\left[\frac{2m}{\hbar^2}(F-V(r))-\frac{\lambda}{r^2}\right]R=0 \qquad (1.6)$$

and

$$\frac{d}{dy}\left((1-\zeta^2)\,\frac{dP}{d\zeta}\right)+\left(\lambda-\frac{m^2}{1-\zeta^2}\right)P=0 \qquad (1.7)$$

These equations have finite solutions for $\lambda=\ell(\ell+1)$ and $|m|\leq\ell$ in the form of the associated Legendre polynomials

$$P_\ell^m(\zeta)=(1-\zeta)^{1/2|m|}\,\frac{d^{|m|}}{d\zeta^{|m|}}\,P_\ell(\zeta) \qquad (1.8)$$

where $P_\ell(\zeta)$ are the Legendre polynomials.

For a finite well where $V(r)=-V_o$ for $r<a$ and $V(r)=0$ for $r>a$ solutions for equation 1.6 may be found. Using

$$\alpha=\left[\frac{2m(V_o-|E|)}{\hbar^2}\right]^{1/2} \qquad r<a \qquad (1.9)$$

$$\beta = \left[\frac{2m|E|}{\hbar^2}\right]^{1/2} \qquad r > a \tag{1.10}$$

and $\rho = \alpha r$ for interior ($r < a$) solutions equation 1.6 simplifies to

$$\frac{d^2R}{d\rho^2} + \frac{2}{\rho}\frac{dR}{d\rho} + \left[1 - \frac{\ell(\ell+1)}{\rho^2}\right] R = 0 \tag{1.11}$$

Solutions are of the form of spherical Bessel functions

$$\ell(\rho) = \left[\frac{\pi}{\partial\rho}\right]^{1/2} J_{\ell+1/2}(\rho) \tag{1.12}$$

and spherical Neumann functions

$$n_\ell(\rho) = [-1]^{\ell+1} \left[\frac{\pi}{2\rho}\right]^{1/2} J_{-\ell-1/2}(\rho) \tag{1.13}$$

The first three terms of each are

$$J_0(\rho) = \frac{\sin\rho}{\rho} \qquad n_0(i\beta r) = -\frac{\cos\rho}{\rho}$$

$$J_1(\rho) = \frac{\sin\rho}{\rho^2} - \frac{\cos\rho}{\rho} \qquad n_1(i\beta r) = -\frac{\cos\rho}{\rho^2} - \frac{\sin\rho}{\rho} \tag{1.14}$$

$$J_2(\rho) = \left(\frac{3}{\rho^3} - \frac{1}{\rho}\right)\sin\rho - \frac{3}{\rho^2}\cos\rho \qquad n_2(d\beta r) = -\left(\frac{3}{\rho^3} - \frac{1}{\rho}\right)\cos\rho - \frac{3}{\rho^2}\sin\rho$$

Because R(r) must be finite at r=0 only spherical Bessel functions are acceptable, and solutions for the interior are $R(r)=Aj_l(\alpha r)$.

For exterior solutions, r>a, both the Bessel and Neumann functions may be employed, and a linear superpostion is found that has the satisfactory exponential fall-off at large r. The desired solutions for r>a are then

$$R(r) = Br_\ell^{(1)}(i\beta r) = B[j_\ell(i\beta r) + in_\ell(i\beta r)] \tag{1.15}$$

whose first three terms are

$$h_0^{(1)}(i\beta r) = \frac{1}{-\beta r} e^{-\beta r}$$

$$h_1^{(1)}(i\beta r) = \left(\frac{1}{\beta r} + \frac{1}{\beta^2 r^2}\right) e^{-\beta r} \tag{1.16}$$

$$h_2^{(1)}(i\beta r) = \left(\frac{1}{\beta r} + \frac{3}{\beta^2 r^2} + \frac{3}{\beta^2 r^3}\right) e^{-\beta r}$$

Energy levels may be obtained by requiring both interior and exterior functions and their first derivatives to be continuous at r=a, which is analogous to requiring that (1/R)(dR/dr) be continuous there. Using $\xi=\alpha a$ and $\eta=\beta a$ this requires the simultaneous constraints of

$$\xi^2 + \eta^2 = \frac{2mV_o a^2}{\hbar^2} \tag{1.17}$$

and each of

l=0:

$$\xi \cot\zeta = -\eta \tag{1.18}$$

l=1:

$$\frac{\cot\xi}{\xi} - \frac{1}{\xi^2} = \frac{1}{\eta} + \frac{1}{\eta^2} \tag{1.19}$$

l=2:

$$-\xi^3\cot\zeta(\eta^2 + 3\eta - 3) - \xi\cot\xi(3\eta^3 + 3\eta^2 - 15\eta) \tag{1.20}$$
$$+ \xi^2(3 + 8\eta - \eta^3) + (3\eta^3 + 3\eta - 15\eta) = 0$$

A graphical presentation of each of these cases is shown in figure 1.1. The intersection of the circle equation 1.17 for each carrier and equation 1.18 is, successively, 1s, 2s etc, and for equation 1.19, 1p, 2p, and so on. The solution for the infinite well case as compared to the finite case is shown in figure 1.2. For the infinite case all energy levels are confined, and the energies are much higher for a given crystallite size. As shown in figure 1.2 by adjusting the crystallite size the 1s-1s energy level may be placed arbitrarily, as in the finite case. However, with a given 1s-1s energy, the energy spacings of the other energy levels are not the same for the finite and infinite cases. The finite well case predicts a 1p-1p transition at lower energies compared to that of the infinite potential case. This is not a critical point at this juncture; the necessity of an energy dependent mass will be discussed subsequently, and this mass will be used as a fitting parameter for the linear absorption. Simply, the infinite well case requires less deviation of the carrier masses away from that of bulk in order to fit the experimental absorptions, but the finite well case is probably nearer the actual condition.

Returning to equation 1.5 where an electric field dissallows separation of the

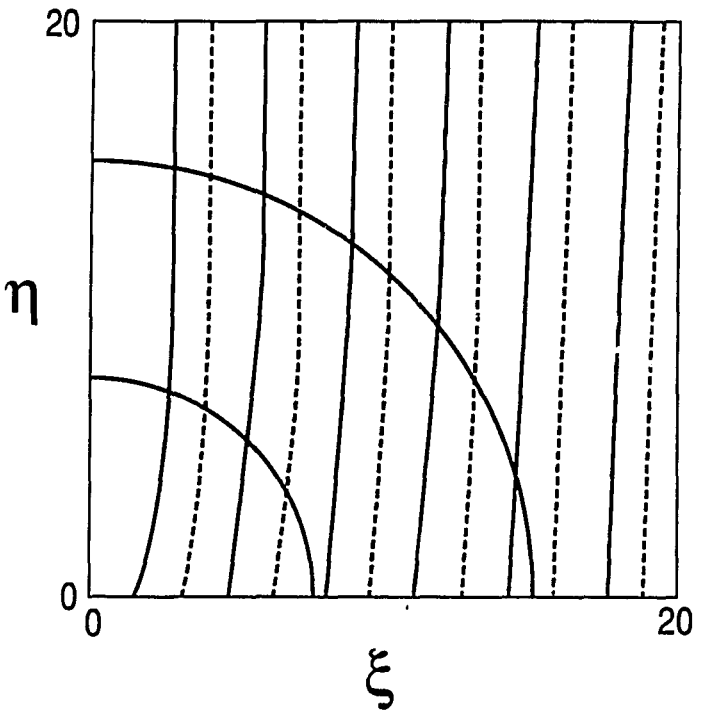

Fig. 1.1 Graphical presentation of solutions for finite well; solid line, l=0; dashed line, l=1.

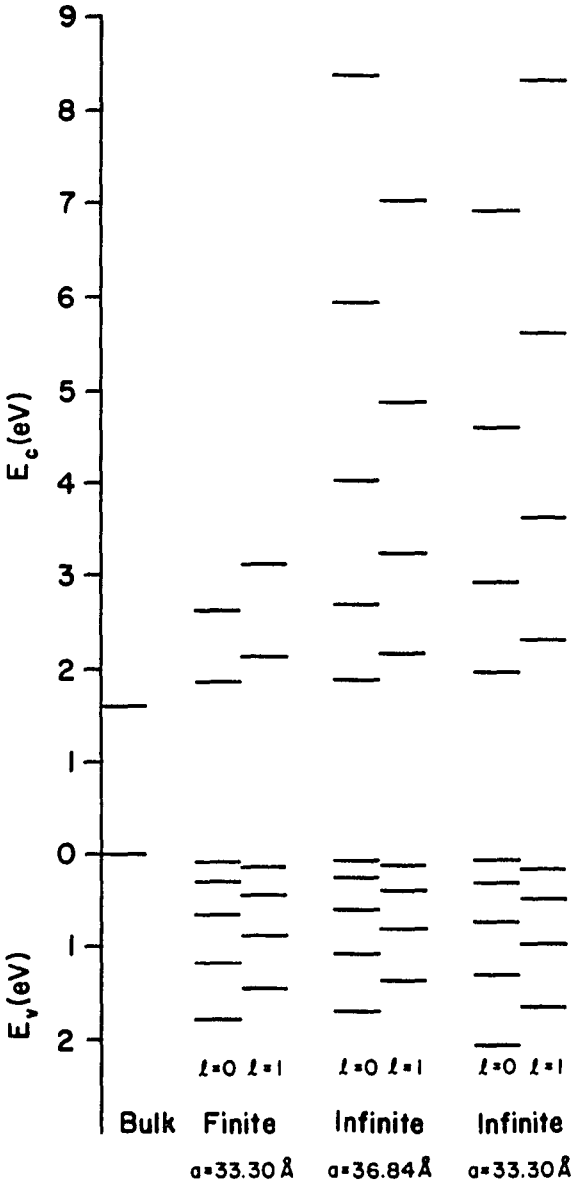

Fig. 1.2 Transition energy levels for finite and infinite confinement, for ℓ=0 and ℓ=1.

wave equation

$$\frac{H}{r^2}\left[\frac{\partial}{\partial r}\left(r^2\,\frac{\partial}{\partial r}\right)+\frac{\partial}{\partial \zeta}(1-\zeta^2)\,\frac{\partial}{\partial \zeta}\right]\chi+\left(Fr\zeta-\frac{H}{r^2}\,\frac{m^2}{(1-\zeta^2)}\right)\chi=\lambda\chi \tag{1.21}$$

solutions may be found as a superposition of the solutions of the F=0 case:

$$\chi=\sum_{n=1}^{nr}\sum_{\ell=0}^{n\zeta} a_{n\ell}^{\ell}\,P_{\ell}^{m}(\eta)\sqrt{\frac{2(\ell+1)(\ell-m)!}{(\ell+m)!}}\sqrt{\frac{\pi}{2r}}\,\frac{J_{\ell+1/2}(K_{\ell,n}r)}{J_{\ell+3/2}(K_{\ell,r}r_o)} \tag{1.22}$$

where $K_{\ell,n}=\phi_{\ell,n}/r_o$, and $\phi_{\Omega,n}$ is the root of the Bessel function for ℓ. Equation (1.22) may also be written as

$$\chi=\sum_{n=1}^{nr}\sum_{\ell=0}^{n\zeta} a_{n\ell}G_{\ell}^{m}(\zeta)B_{\ell}^{\eta}(r) \tag{1.23}$$

where

$$a_{n\ell}=\frac{1}{\sqrt{r_0 2\pi'}}\,a'_{n\ell} \tag{1.24}$$

$$G_{\ell}^{m}(\zeta)=\sqrt{\frac{(2\ell+1)(\ell-m)!}{(\ell+m)!}}\,P_{\ell}^{m}(\zeta) \tag{1.25}$$

and

$$P_{\ell}^{m}(\zeta) = [1 - \zeta^2]^{|m|/2} \frac{d^{|m|}}{d\zeta^{|m|}} \left[\frac{1}{2^{\ell}\ell!} \frac{d^{\ell}}{d\zeta^{\ell}} [\zeta^2 - 1]^{\ell} \right] \tag{1.26}$$

are the associated Legendre polynomials. Also

$$B_{\ell}^{n}(r) = \frac{j_{\ell}(K_{\ell,n} r)}{j_{\ell+1}(K_{\ell,n} r_o)} \tag{1.27}$$

with

$$j_{\ell}(K_{\ell,n} r) = \sqrt{\frac{\pi}{\partial r K_{\ell n}}} J_{n+1/2}(K_{\ell,n} r) \tag{1.28}$$

$$j_{\ell+1}(K_{\ell,n} r_o) = \sqrt{\frac{\pi}{\partial r K_{\ell n}}} J_{n+3/2}(K_{\ell,n} r_o) \tag{1.29}$$

Substituting 1.23 into 1.21 the eigenvalue equation

$$Ca = \lambda Da \tag{1.30}$$

is found, where $a=a_{nl}$ is the eigenfunction with corresponding eigenvalues. By diagonalization the eigenfunctions and eigenvalues are found with an electric field. When F=0 the eigenvalue energies of equations 1.17 through 1.20, with an infinite potential (equation 1.22), are found.

The absorption with various values of F, including F=0 V/cm, were obtained by using

$$\alpha \propto \sum_{\substack{n\ n' \\ \ell\ \ell' \\ m\ m'}} a_{n\ell m}\psi^{e}_{n\ell m}a_{n'\ell' m'}\psi^{h}_{n'\ell' m'}\delta(E_g - E^e - E^h) \qquad (1.31)$$

The relative magnitude and positions of the absorption peaks are shown in figure 1.3 for $F=10^5$ V/cm and F=0 V/cm (using a crystallite radius of 35Å, $m_e=.1$, $m_h=.4$, consistant with CdTe). The main result of an applied field is the red shift of the 1s-1s transition and the opening up of previously dissallowed states ($\Delta\ell\neq0$, $\Delta n\neq0$). Wavefunction mixing reduces the F=0 quantum confined transitions and opens up transitions which increases absorption between the original states.

It is found that the above equations, with constant carrier masses for the electrons and holes, results in predicted enegy level postions that are smaller than those observed in the measured linear absorption. This is not at all surprising in light of the substantial energy shifts encountered in these quantum confined systems, and the fact that effective masses are not at all constant as a function of energy. The bands may only be usefully approximated as parabolic very close to k=0. With shifts of from .5eV up to over 1eV from the bulk band gap, wide variations of the electron and hole masses are certain to occur.

Figure 1.4 shows the band diagrams for CdS [Cohen et al. (1967)] and CdTe [Chadi et al. (1972)]. It is apparent that for all but very small energies about the band gap energy, large variations of the effective mass, including sign changes and values approaching ∞, may occur.

The fitting of the linear absorption for CdTe was attempted more fully in order to investigate other phenomena, to be described in later sections, and because the

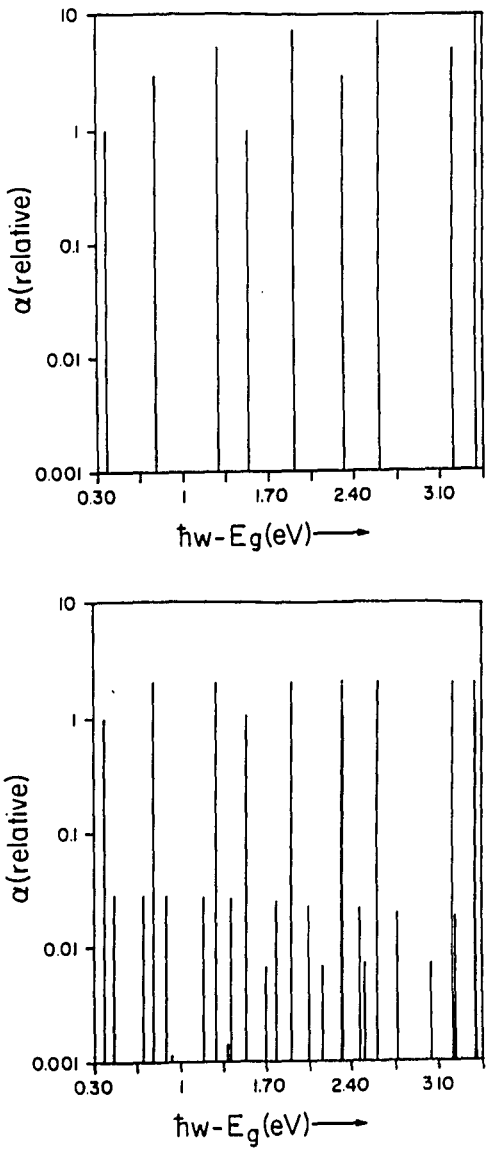

Fig. 1.3 Magnitude and position of absorption features for F=0, F=10^5.

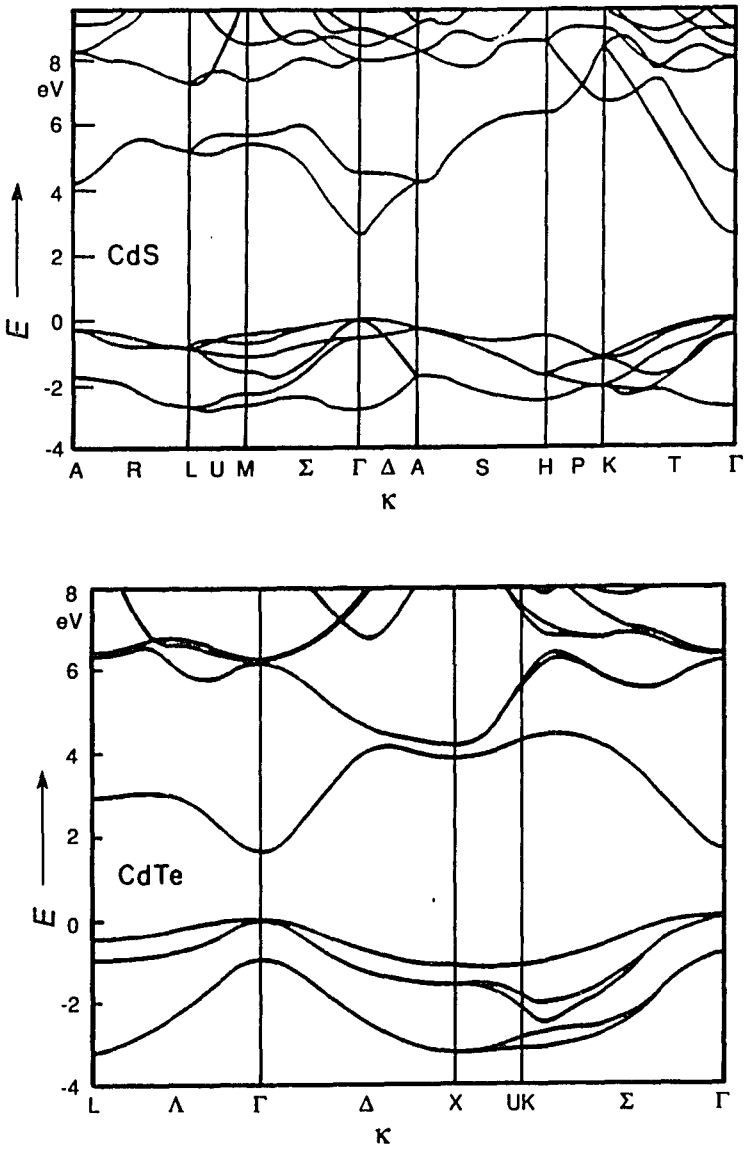

Fig. 1.4 Band diagrams for CdS [Cohen et al. (1967)] and CdTe [Chadi et al (1972)].

absorption displayed many more quantum confined features, which allowed varification of effects over larger energy intervals. The transition diagram shown in figure 1.5 was assumed. As a simplifying assumption the b hole band, degenerate in bulk, was neglected, noting that the absorption due to it appears to be small in comparison to the a band. The c hole band was neglected because its energy levels are shifted to about 400 nm, and its absorption is small. Values for the mass of the electron as a function of energy were estimated from an examination of the band diagram. Clearly the electron, and hole, bands open up as energy increases, that is , the energy tends toward a constant value as k increases away from the Γ point. Thus masses increase as energy shifts increase, and values can be estimated from the band diagram (albeit trusting in their accurate calculation and their applicability in crystallites not necessarily bulk like in their structure). Because of the much smaller energy shifts experienced by the hole, due to its heavier mass, the hole mass was taken as a constant.

The measured linear absorption was also substantially broadened by inhomogeneous and homogeneous broadening. In order to model this a Gaussian line shape was assumed, with increasing width with increasing energy shift, consistent with a shorter lifetime for higher energy levels. In summary, the values used to fit the linear absorption of sample 650-.5 were: Gaussian linewidths in meV for $n_e = 1$, $\ell_e = 0,\ldots, 5$ and $n_e = 2$, $\ell = 0,\ldots,3$ respectively: 70, 180, 210, 240, 300; 230, 270, 340, 360 independent of n_h , ℓ_h except $n_h = 1$, $\ell_h = 1$ to $n_e = 1$, $\ell_e = 0$ was assigned 150 meV. Similarly, m_e/m_0 : 0.103, 0.138, 0.152, 0.163, 0.173, 0.179; 0.156, 0.169, 0.178, 0.180, 0.180, 0.180 and $m_h/m_0 = 0.4$ throughout. The resultant calculated absorption, along with the measured α for the sample, are shown in figure 1.5 .

Although this fitting procedure is 'hand waved', using quite reasonable assumptions concerning obvious considerations, the actual verification of its usefulness is

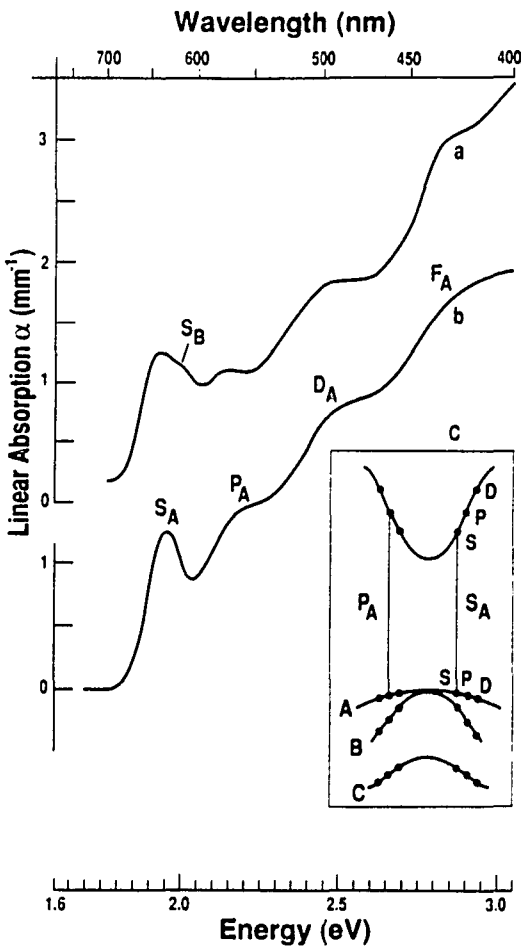

Fig. 1.5 Calculated (a) and measured (b) linear absorption for CdTe.

the ability with which the quantum confined Franz-Keldysh is modeled using these same parameters, as disscussed in chapter 3.

Growth of Microcrystallites in Glass

The growth of microcrystallites in glass has been thoroughly investigated theoretically [Lifshitz, Slezov (1961)], and instances of experimental verification have occurred [Ekimov et al. (1985)]. However, many cases of successful growth have not, apparently, led to $t^{1/3}$ growth dynamics and or the predicted Lifshitz-Slezov size distribution.

The actual mechanism which produces the crystallite growth is due to the solubility related curvature of microcrystallite spheres (or nonspherical structures) as described by the Thomson-Freundlich relationship [Potter (1988)]. Large semiconductor solute concentrations are found near high curvature, small crystallites; and low concentrations near low curvature, large crystallites. The concentration gradient drives the solute toward the larger crystallites where adhession produces growth. Thus larger crystallites consume smaller crystallites.

Through the theoretical treatment of this mechanism the average crystallite size has been predicted as

$$R_{av}^3(A) = \frac{4}{9} D\alpha t \qquad (1.32)$$

where D is the diffusion coefficient, α is interphase surface tension $\alpha=(\sigma/k\tau)VC_\infty$, V is the atomic volume, and C_∞ is saturated solution concentration.

The size distribution is also derived and is found to be

$$P(u) = \frac{3^4 e u^2 \exp(-1/(1 - 2u/3))}{2^{5/3}(u + 3)^{7/3}(3/2 - u)^{11/3}} \qquad u < 1.5 \qquad (1.33)$$

$$P(u) = 0 \qquad u > 1.5$$

and is shown in figure 1.6. It is notable at this point that the Lifshitz-Slezov size distribution predicts a full width half maximum crystallite size distribution of about R/R_{av}= 1, -.15, +.25 .

These expressions are given as a basis to compare the quantum dot microcrystallites grown and investigated in the course of the described experiments and those grown by others.

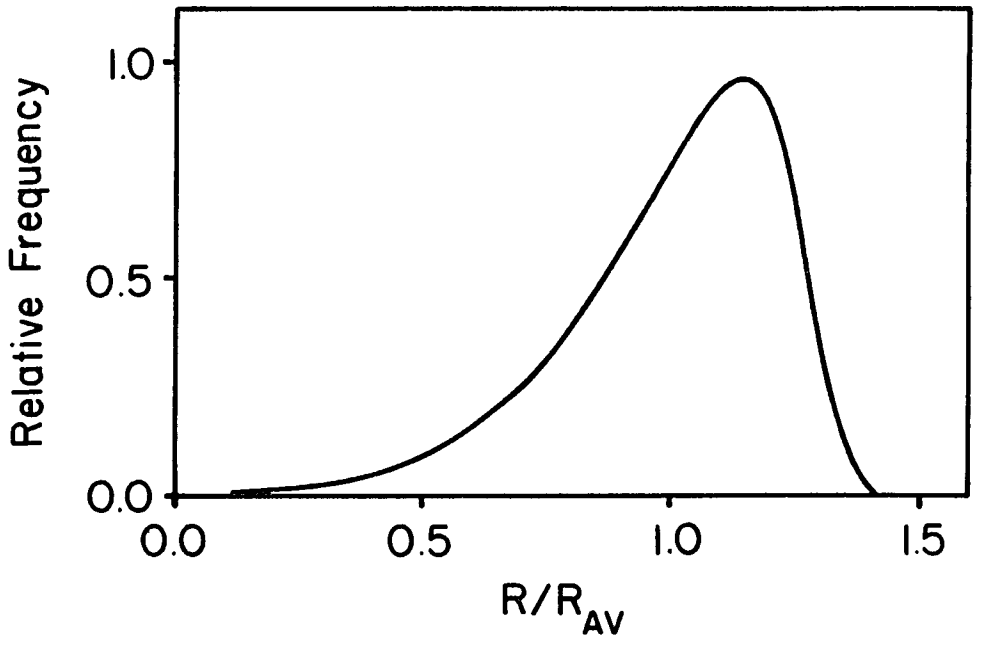

Fig. 1.6 The Lifshitz-Slezov crystallite size distribution.

CHAPTER II

GROWTH AND LINEAR ABSORPTION

The linear absorption of the microcrystallites grown in glass was measured for CdS and CdTe. The temperature dependence of the 1s-1s transition was found to be the same as bulk, and the 1s-1s linewidth demonstrated crystallite size dependent behavior. The fluorescence for CdTe and CdS was also measured, giving evidence for different trap state configurations. For CdS, relative magnitudes of trap state fluorescence changed with crystallite size.

The growth procedure was optimized using quantum confined behavior as the criteria, and the trends of quantum confined behavior with growth conditions were determined. The growth dynamics appear to be well behaved under certain conditions, but agreement with accepted theory was not found.

Growth

The growth of semiconductor microcrystallites (growth was performed by L.C. Liu and S.H. Risbud of the Department of Materials Science and Engineering, University of Arizona) in the glass can be divided up into two processes; the glass synthesis and melting, and the nucleation and mass transport whereby larger crystallites grow at the expense of smaller ones. Ideally the melting process uniformly mixes all the glass constituents and the semiconductor (added in crystalline powder form). The

melting temperature must be compatible with all the glass constituents, necessary for proper glass behavior, and the semiconductor. It is preferrable that the melt be stirred (with, for example, a platinum paddle at 20 rpm) to enhance uniformity, but this is not always practical, especially in small capacity experimental run ovens. Convective currents help to move the material around in any case.

After an appropriate melting period the material is removed from the oven and rapidly quenched to room temperature on a brass plate to prevent nucleation of crystallites. The glass is now optically clear and supersaturated with the semiconductor. The sample is then given a short low temperature annealing to remove strain so that several smaller samples can be cut from a single melt block for growth annealing.

These samples are then heat treated for various times and temperatures. During this growth annealing period the semiconductor atomic oxides nucleate to crystalline semiconductor sites. Also the process takes place by which small crystallites are dissociated and larger crystallites grow from the material thus made available, as described in chapter one.

The growth of the microcrystallites is sensitive to many factors, including the glass constituents and the growth annealing. The process by which the base glass is chosen is not prescriptive, being a combination of chemistry and experience. The choice of the base glass is followed by that of flux modifiers that variously affect the physical properties of the glass (viscosity, glass forming character etc) and the compatibility with the particular semiconductor (including solubility, impurity incorporation, microcrystallite formation, melting temperatures and vapor pressures, etc). Two slightly different glasses were found for the growth of CdS and CdTe microcrystallites.

By the described general method CdS and CdTe microcrystallite 'quantum dot'

samples were successfully grown. The growth parameters are shown in table 2.1.

The semiconductor doped glasses were optimized using the absorption spectra as the primary criteria, i.e. good quantum confined features and large band edge shifts. The trend, demonstrated primarily in the CdS samples due to their higher degree of material development at this time, showed that in general longer-duration lower-temperature growth annealings provide better quantum-confined behavior and growth predictability (figure 2.1). The data for these figures were taken from samples displaying clearly discernible linear absorption 1s-1s peaks. Figure 2.2 shows the progression from base glass absorption to a well confined absorption feature for the 590° C anneal series. The definition of short and long time, or high and low temperature for the annealing depends on the glass-semiconductor system. The CdS and CdTe systems seem to be quite different in this respect. With higher temperature short time runs the quantum confined character cannot be predicted before hand, and there are indications that these samples may be different from an optical properties standpoint compared to long time low temperature samples, even though they may exhibit good linear absorption quantum-confined features.

The crystallite size for some samples of CdS, as determined by the energy shift using an infinite well, is plotted versus $t^{1/3}$ in figure 2.3. The growth character does not fit that predicted by equation 1-32. The trend is linear versus $t^{1/3}$, but the lines do not pass through t=0, a=0, or any other common point for that matter. It is apparent that there is crystallite size offset in all cases. Lifshitz and Slezov have allowed for an initial crystallite radius, presumably from undissolved semiconductor material or crystallites nucleated in the initial cooling process after glass mixture. They point out that growth may proceed from this initial size if a nonequilibrium supersaturation is present, and this proceeds until the excess supersaturation is expended in growth. The

	CdS	CdTe
Glass Comp (wt%):		
SiO_2	56	54.2
B_2O_3	8	23.3
K_2O	24	6.6
CaO	3	0.8
BaO	9	2.5
ZnO		9.8
Na_2O		1.8
Al_2O_3		1.0
Semiconductor (wt%)	0.5	2-3
Melt temp. (°C)	1400	1200
Melt time (hrs)	2	1
Growth anneal (°C)	590-700	600-700
Growth time (hrs)	140-0.25	1-0.25

Table 2.1 Growth parameters for CdS and CdTe.

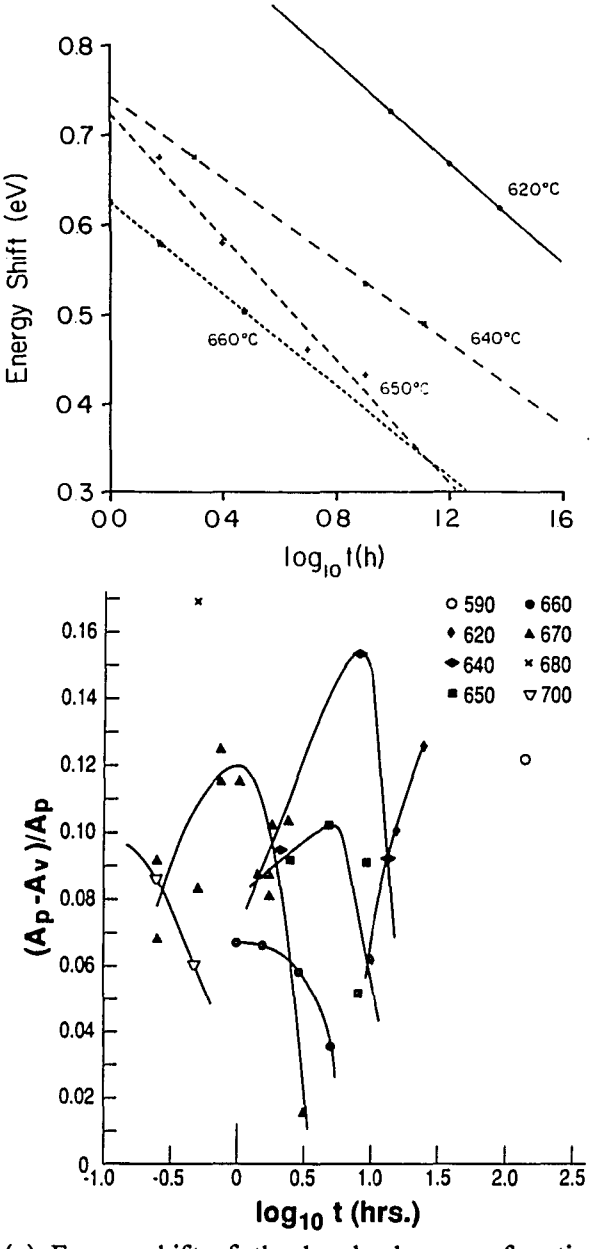

Fig. 2.1 (a) Energy shift of the band edge as a function of growth duration for several temperatures. (b) Peak (A_p) to valley (A_v) ratio as a fraction of 1s-1s absorption peak.

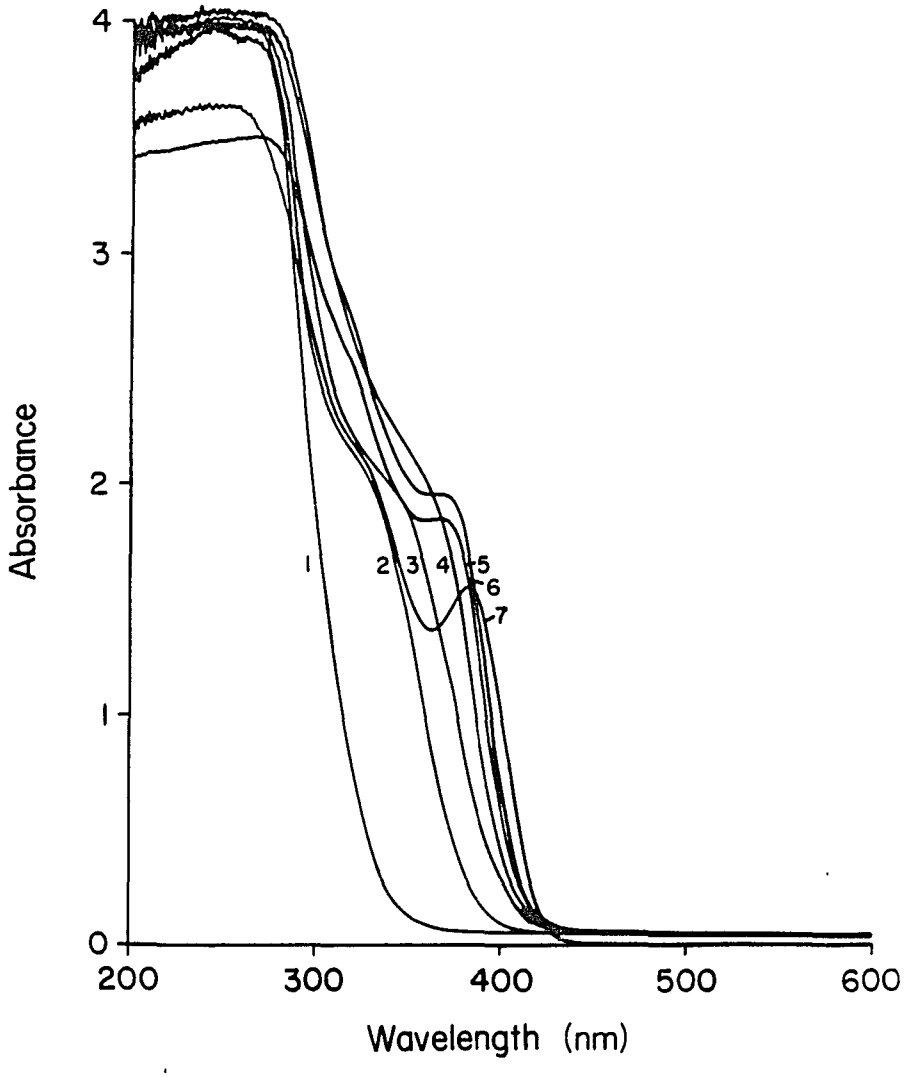

Fig. 2.2 Linear absorption for the annealing series of 590°C, for various annealing times: for curves 1 to 8; 4, 12, 26, 38, 53, 65, 140 hours respectively.

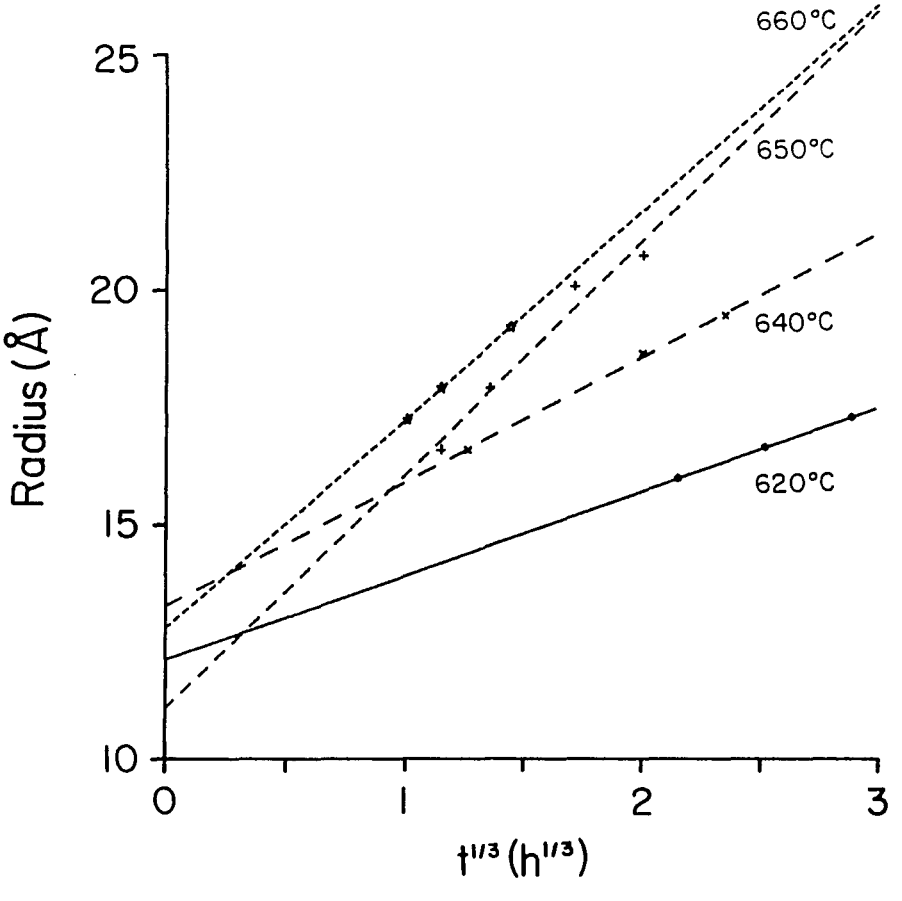

Fig. 2.3 Crystallite size, as calculated from an infinite well model, versus $t^{1/3}$.

very small concentrations of semiconductor initially present in the glass make the true cause of the rapid growth, or existing crystallite distribution, at short times unclear.

Linear Absorption

The linear absorption spectra of several samples (sample nomenclature: 590-140 means a sample growth annealing of 140 hours at 590°C) of CdS microcrystallites in glass, at several temperatures, are shown in figure 2.4, and for a CdTe sample in figure 2.5. As can be seen both quantum dot types show significant quantum-confined character. Using a finite potential model the features (quantum confined) imply a crystallite radius of from 13.5Å to 21.8Å for CdS and 33.3Å for CdTe. As discussed in chapter 1, the linear absorption has been modeled for the case of CdTe.

The linear absorption was investigated as a function of temperature [Esch et al. (1989)] to see the nature of the phonon interaction with these very small crystal structures. It has been noted that the bulk crystal structure is not achieved below some crystal size (approx. 1000 atoms [Brus (1984)]) and hence it is reasonable to speculate that the phonon interaction in the crystallites might differ from that of the bulk.

The shift of the band edge due to the finite phonon population and expansion of the lattice is very well known [Ashcroft, Mermin (1976)]. The red shift in bulk is quadratic in temperature at low temperatures, and linear thereafter. The shift of the 1s-1s transition as a function of temperature was found to be the same as that in bulk (figure 2.6 for CdS and figure 2.7 for CdTe).

The fluorescence structure of the CdS samples, shown in figure 2.8, was found to be consistent with that observed by others, although theirs was a vastly different system (superclusters in zeolites) [Wang et al. (1989)]. The relative strengths of the peaks was

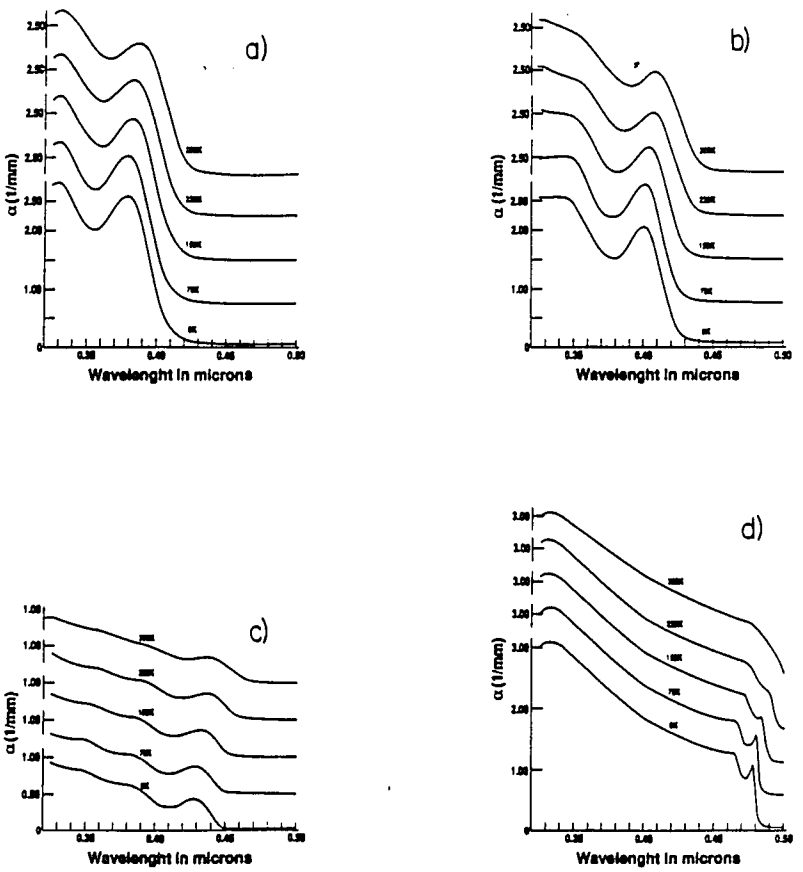

Fig. 2.4 Linear absorption at several temperatures for different CdS samples: (a) sample 590-140 (r=13.5Å), (b) 640-4 (r=16.5Å), (c) 670-.5 (r=21.8Å) (d) 700-1 (bulk like).

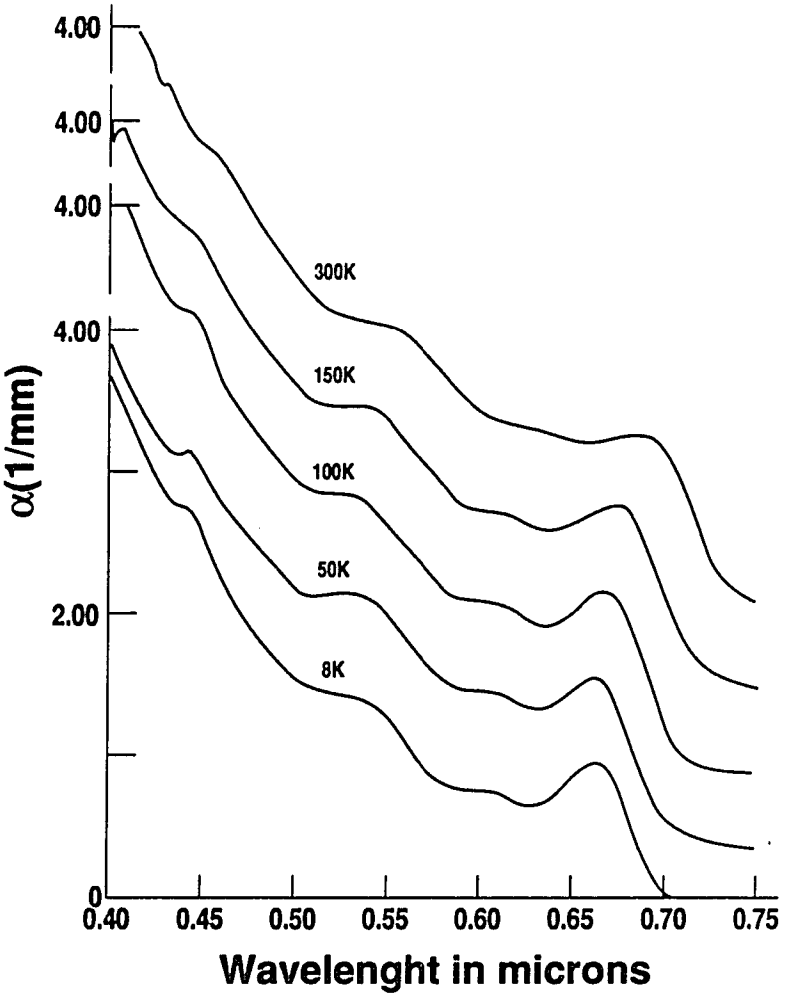

Fig. 2.5 Linear absorption at several temperatures for a CdTe quantum dot sample.

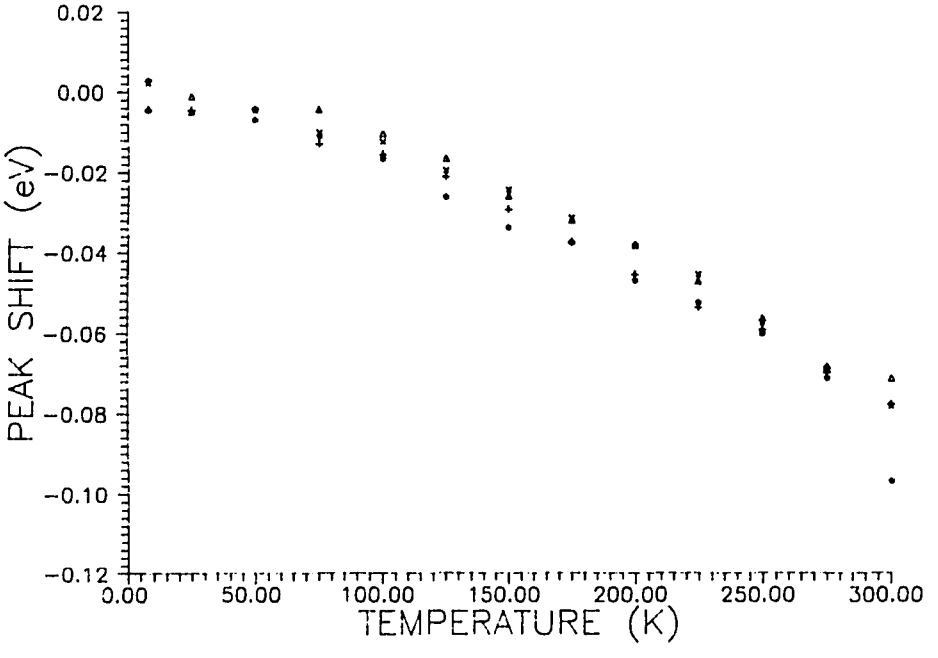

Fig. 2.6 Shift of the band edge as a function of temperature for CdS quantum dot sample (for the samples of figure 2.4).

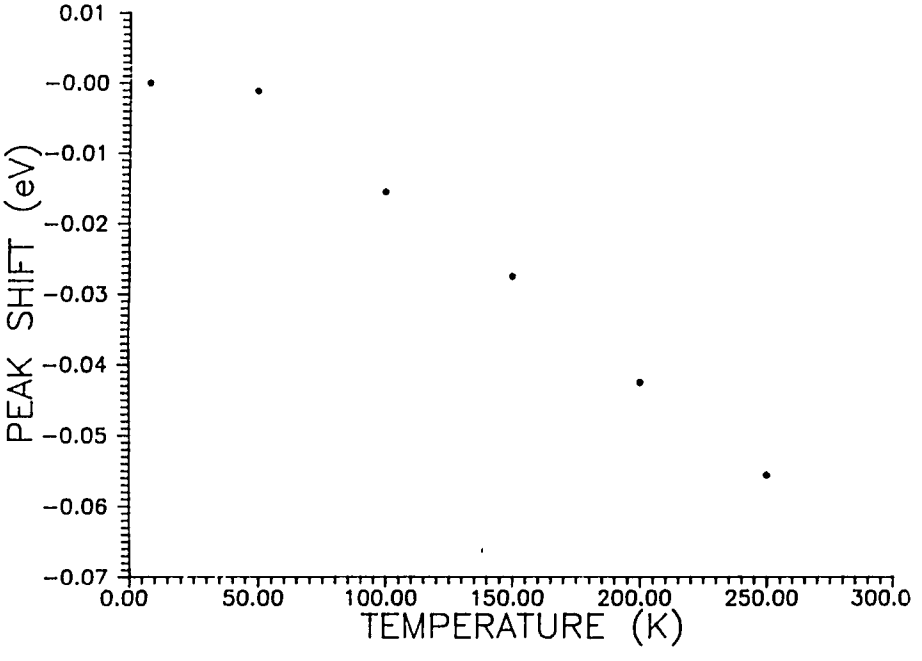

Fig. 2.7 Shift of the band edge as a function of temperature for a CdTe quantum dot sample.

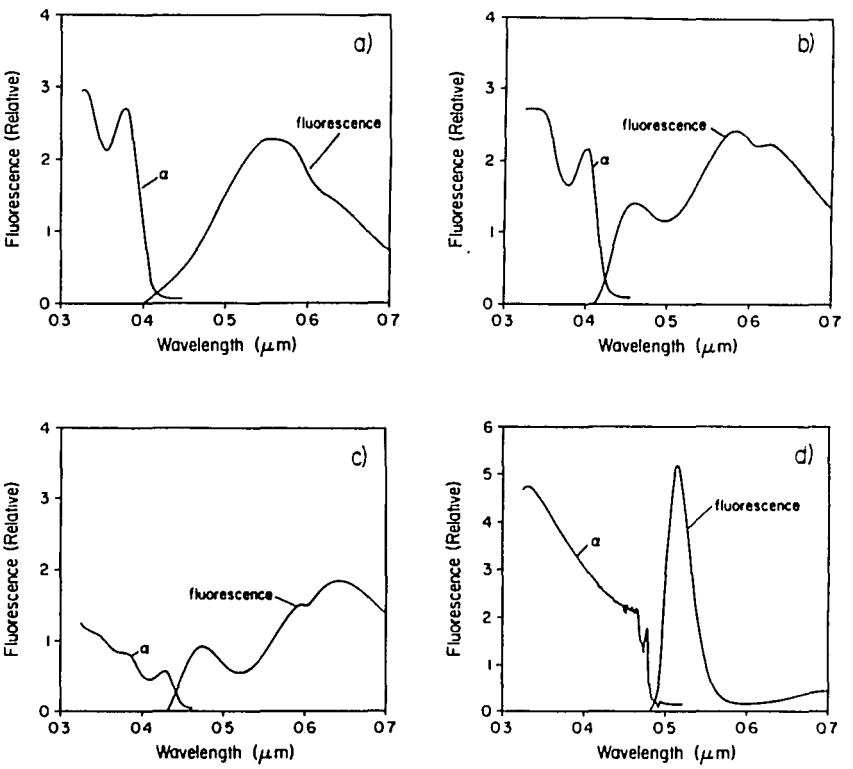

Fig. 2.8 Fluorescence for several CdS samples, at 8K: (a) sample 590-140, (b) 640-4, (c) 670-.5, (d) 700-1.

highly dependent on the size of the crystallites involved. All the peaks have been attributed to defects, respectively from blue to red, a sulfur related defect, Cd atoms, and a sulfur vacancy. It is notable from figure 2.8 that the Cd atom defect seems to dominate with smaller crystallite size, and the sulfur related defect with larger crystallite size, which may imply the Cd defect is associated with the surface, and the sulfer defect with the volume. The fluorescence exhibits a large shift from the 1s-1s absorption feature, and in fact no fluorescence signal is observed that would indicate direct 1s-1s recombination in either CdS or CdTe. The observed signal for CdTe is shown in figure 2.9, and in this case the fluorescence signal is closer to the absorption peak, being centered 60 meV away from the excitation energy (when excited in the 1s-1s peak). The fluorescence has been observed not to shift with shifting pump wavelength for the case of CdS, which is in contrast to the behavior observed in CdTe, where the 60 meV seperation of pump energy and fluorescence peak is observed independent of pump position within the 1s-1s absorption peak. The significant implications of the fluorescence signal with respect to pump probe differential absorption signals, particularly for the case of CdTe, will be discussed more fully in chapter 4.

The linewidth associated with the LO phonon interaction is given by

$$\Gamma=\Gamma_o+\frac{\Gamma_{ph}}{\exp(h\Omega_{LO}/kT)-1}$$

where Γ_o is the constant inhomogeneous term, Ω_{LO} is the LO phonon energy, and Γ_{ph} is a phonon broadening coefficient [Weiner et al. (1985)]. The linewidth of CdS is shown in figure 2.10. The model indicates different values of Γ_o and Γ_{ph} for each sample. This demonstrates an increasing homogeneous linewidth with decreasing crystallite size,

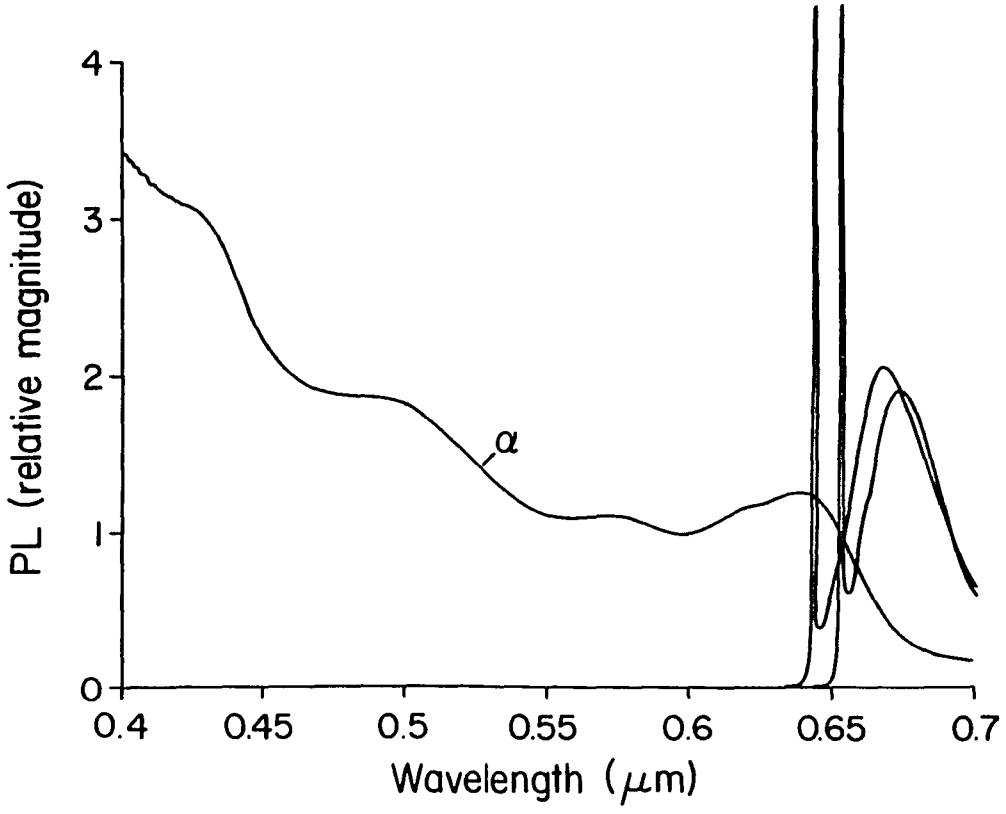

Fig. 2.9 Fluorescence for a CdTe sample, at 8K, for two different pump wavelengths (not simultaneously).

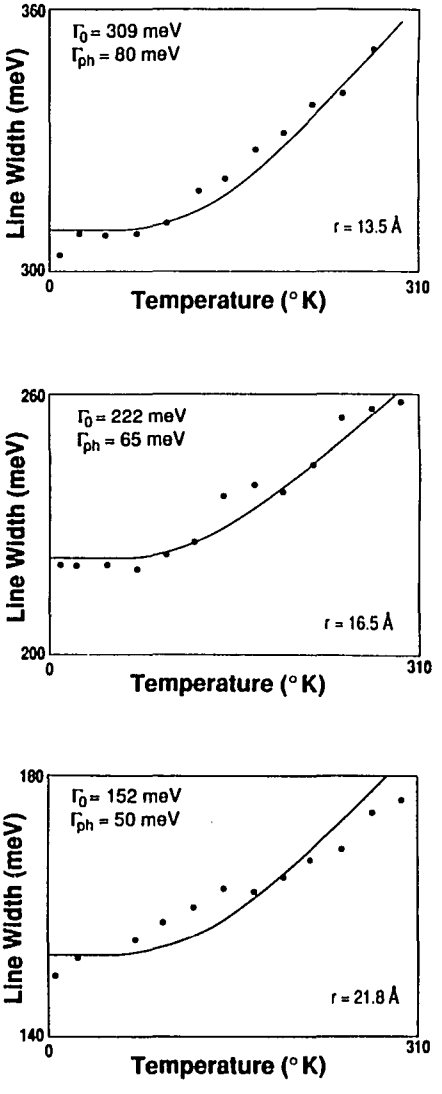

Fig. 2.10 Linewidth as a function of temperature for several CdS samples: top, sample 590-140; middle, 640-4; bottom, 670-.5.

consistent with trends demonstrated in other quantum-confined systems (as observed in quantum well structures). An increased phonon coupling is also indicated for the smaller crystallites. Note that although sample 670-.5 is consistent with the trends indicated it does not show the Frohlich behavior and in fact it appears linear. However, the sample is exceptional for several reasons. It was grown under short-time/high-temperature conditions, which implies unpredictable growth behavior, it demonstrated the largest quantum confined crystallite size grown, and its integrated absorption was low in comparison to other samples (same initial CdS concentration in the melt).

The nature of the linewidth of the quantum confined features is of particular interest and so it is instructive to consider the crystallite size distribution implied by the 1s-1s peak linewidth, especially in CdS samples. If one assumes no homogeneous linewidth then the entire linewidth may be attributed to the 1s-1s level energy distribution caused by the crystallite size distribution. For the case of CdS sample 640-4, with a 1s-1s peak energy at 8K of 3.1eV (400nm) $\pm\simeq$.125eV, the finite well model dictates a crystallite radius of 16.5 ±2.5Å . The Lifshitz-Slezov size distribution, as expressed in equation 1.33, predicts a radius distribution at full width-half maximum of approximately R/R_{av}= 1, -.15, +.25, which is 16.5Å, -2.5Å, +4.1Å . It appears that the actual crystallite size distributions were slightly smaller than that predicted by theory. The radius fluctuation measured, and predicted by the Lifshitz-Slezov distribution, is less than the bulk lattice parameters (for the hexagonal; a: 4.1Å, c: 6.7Å).

CHAPTER III

QUANTUM CONFINED FRANZ-KELDYSH EFFECT

The electroabsorptive effect in MQW structures has been the subject of much interest, and is the basis of the well known SEED device [Miller et al. (1984)]. The effect of an electric field on a quantum dot system has also drawn interest due to the possibility of lower device switching energies [Miller et al. (1988)]. The quantum confined Franz-Keldysh (QCFK) effect [Hache et al. (1989)], so named due to the neglect of coulombic interactions in its theoretical description, was modeled for CdTe using the parameters used to fit the linear absorption, as described in chapter 1. Experimental measurements with CdTe show remarkable agreement. Measurements were also made for bulk-like microcrystallites of CdTe, as well as CdS quantum dots.

Model

Using the electric field wave equation and the eigenvalue equation as presented in chapter 1, and using the parameters used to fit the linear absorption as there described, the QCFK signal may be calculated. Infinitly high potential barriers were assumed and the coulombic interaction neglected. As discussed in chapter 1 the main result of the electric field is the red shift of the 1s-1s transition, and the opening of previously disallowed transitions. The calculated $\Delta\alpha$ spectrum is shown in figure 3.1a.

In addition to a uniform electric field, the effect of point charges on the quantum

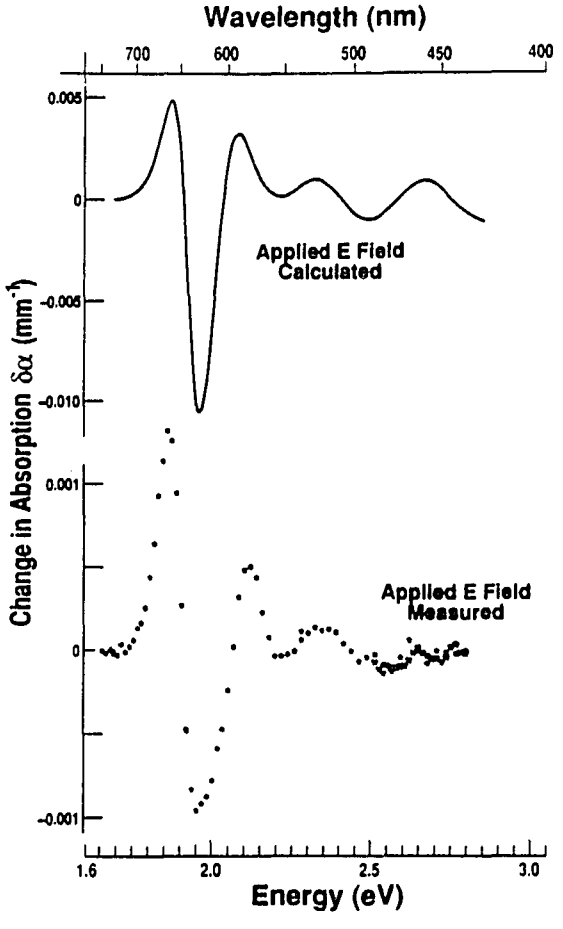

Fig. 3.1 The quantum confined Franz-Keldysh effect in CdTe quantum dots: (a) Calculated spectrum, (b) Experimentally measured spectrum.

dot absorption was investigated. For +e at z = 1.1 r_0 and -e at z= -1.1 r_0 the $\delta\alpha$ spectrum is indistiguishable from that of figure 3.1a. Some charge locations can produce distinguishable $\delta\alpha$, including spectra that lack the low energy increasing absorption feature (and appear similar to the $\delta\alpha$ obtained by photo-excitation; see chapter 4).

Measurement

The excedingly small magnitude ($\simeq$0.1%) of the QCFK effect made measurement an exacting procedure. To provide sufficient interaction length the sample was configured in a waveguide, and the field was applied transverse to the light propagation direction (figure 3.2). The sample ends were polished flat and reasonably square, and then the samples, originally 1 to 2 mm in thickness, were ground and polished to the desired 100 to 200 μm thickness. A high quality surface was necessary on the transverse sides as any surface roughness tended to cause current paths and arcing, which led to catastrophic sample failure.

Approximately 10 nm thick silver electrodes were applied to the sample center using a mask, keeping about 1 mm seperation from the sample edges. Silver paint was used as an adhesive and electrode to mount the sample to a special cold finger adapter for the LT3-110 APD Cryogenics helium dewar The voltage leads were supplied through a vacuum feed-through and the exposed wires, subject to condensation during use of the dewar, were insulated with Apiezon Q.

The applied voltage, of up to 2 kV, was modulated at 50 Hz, using a Kepco operational amplifier, so that drift and instability could be averaged out during data taking. Gated photon counting, with voltage on and off, was done in synchronization

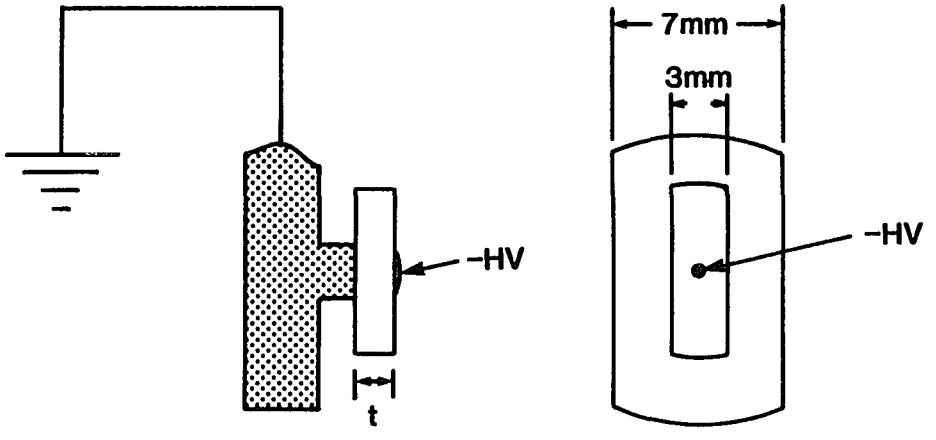

Fig. 3.2 Experimental configuration of sample.

with the applied voltage.

Because stability was paramount in this experiment any noise or wander in the probe source was of particular concern. The xenon lamp, used for other measurements, was completely unacceptable in this respect, as were several other 'high stability' sources and power supplies. A stabilizing detector feedback circuit were finally used (appendix C) with a 12 V filament lamp to provide an exceptional .001% stability. The filament lamp, generally unacceptable due to its low irradiance, was advantageous in this case because the filament length could be imaged upon the length of the sample, providing good throughput, and again onto the slit of the spectrometer.

Again due to the very small signal size any nonlinearity in the photon counting discrimination circuits had to be avoided. A range of acceptable count rates, known to give linear response, was established, and multiple wavelength scan regions that stayed within this range for a given spectrometer slit width were used. Spectrometer slits were adjusted to manipulate the signal seen by the PMT into the acceptable range.

To calculate the actual electric field inside the microcrystallites the effect of the dielectric constants had to be included. By using

$$E_{in} = \frac{3\epsilon_1}{2\epsilon_1+\epsilon_2} E_o$$

where ϵ_1=5 and ϵ_2=10 are the dc dielectric constants, an externally applied field of 2 kV on a sample 125 μm thick produces an electric field of 58 kV/cm in the microcrystallite.

Figure 3.1b shows the measured QCFK effect $\Delta\alpha$ for CdTe. The agreement with theory is very good, especially considering the simplifying assumptions and paramerters used to fit the linear absorption which is the unperturbed spectrum for the QCFK

calculation. The effect of the electric field strength was examined at several points on the curve, and the required quadratic behavior was verified.

To further verify the effect and to provide continuity with the bulk Franz-Keldysh effect, the electric field effect was measured on a CdTe microcrystallite sample where the crystallite size was large compared to the exciton Bohr radius, and the sample displayed bulk absorption characteristics. Figure 3.3 displays the $\Delta\alpha$ (band gap at 1.6 eV) and it is identical to Franz-Keldysh measurements made in bulk semiconductor materials.

An attempt was made to observe the QCFK effect in CdS quantum dot glass samples, with vastly different results. Figure 3.4 shows the $\Delta\alpha$ spectra for a sample with a 1s-1s absorption feature at 3.06 eV (absorption $\simeq$0 at 2.95 eV) and only a large increasing absorption feature is apparent. No other features were observed at higher energies. There is no explanation for this at present, but the difference may have something to do with the difference in trap state configuration and mechanism between CdTe and CdS. A significant difference has been seen in the fluorescence signals, as disscused in chapter 2 and chapter 4. It is possible that the electric field enhances trap state absorption in CdS, resulting in the measured signal, and possibly canceling to some extent the field within the dot.

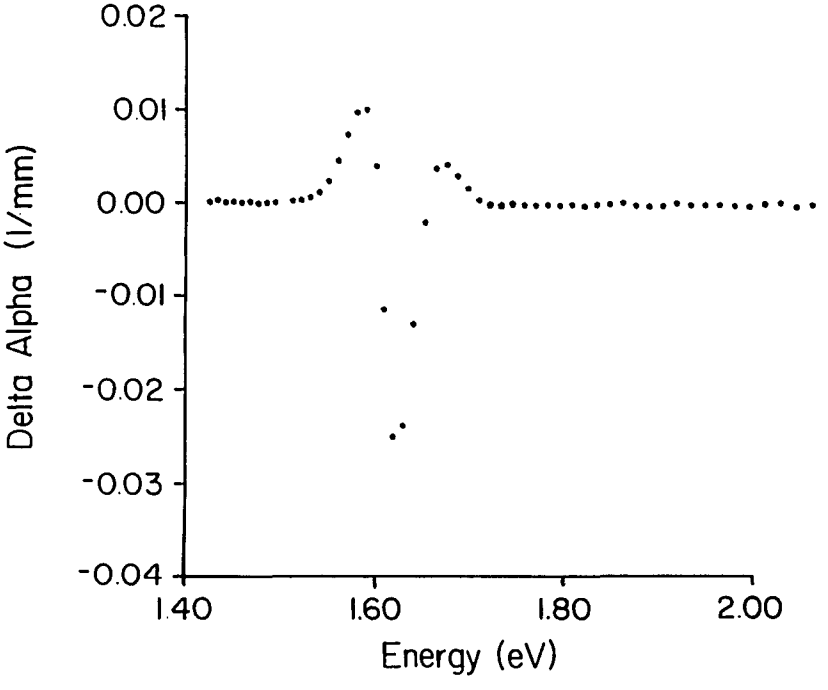

Fig. 3.3 Franz-Keldysh effect as measured on large crystallites with bulk-like absorption character (band gap at 1.6 eV).

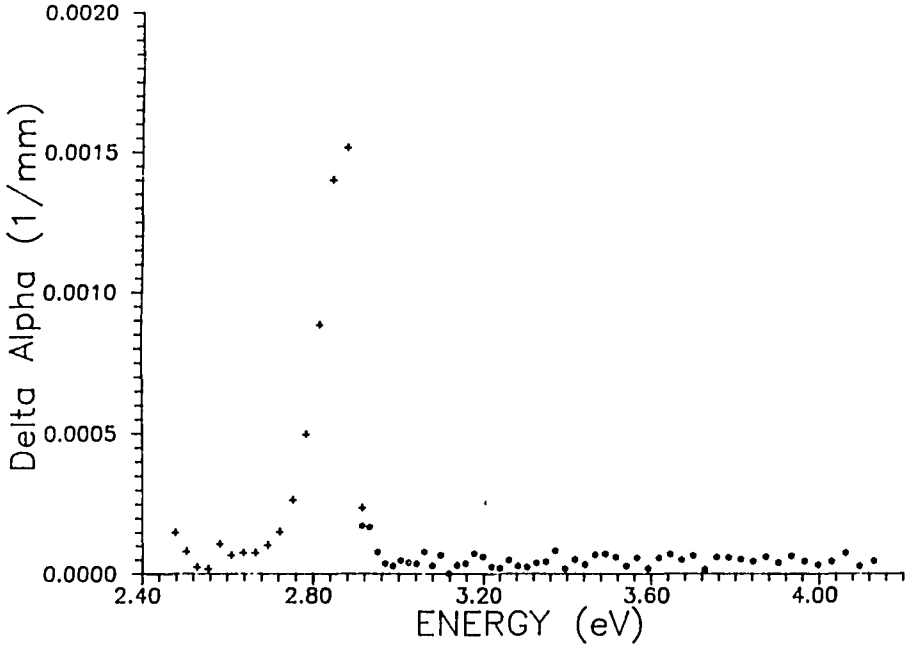

Fig. 3.4 Electric field effect on CdS quantum dot sample (1s-1s transition at 3.06 eV, absorption ≃0 at 2.95 eV).

CHAPTER IV

NONLINEAR OPTICAL PROPERTIES

Differential absorption measurements, using pump-probe techniques, were originally undertaken to determine the homogeneous linewidth of the microcrystallite absorption. The behavior of the differential signals using nanosecond and microsecond excitation, particularly their lifetime, were inconsistent with accepted explanations of the mechanisms responsible for the nonlinear absorption, namely pure phase space filling. The initial observations led to considerable efforts to clarify the nature of the responsible effects.

Nanosecond Differential Transmission

Very high peak powers were used to pump both CdTe and CdS using a tripled Nd:YAG based dye laser (in collaboration with Koo Kang and Nasser Peyghambarian). The system was best suited for CdS because of available pump wavelengths. The experimental setup is shown in figure 4.1 . (DAS is Differential Absorption Spectrum, or simply $\Delta\alpha$; DTS is Differential Transmission Spectrum, DTS=$(T'-T_0)/T_0$, where T' is the pumped transmission and T_0 is the unperturbed transmission. For small DTS, DTS$\simeq -\Delta\alpha L$.) The samples were probed with about a 10 ns broad band dye fluorescence pulse, from a dye cell pumped by the third harmonic of a Q-switched Nd:YAG laser. The sample was pumped off-axis, for isolation from the probe optical

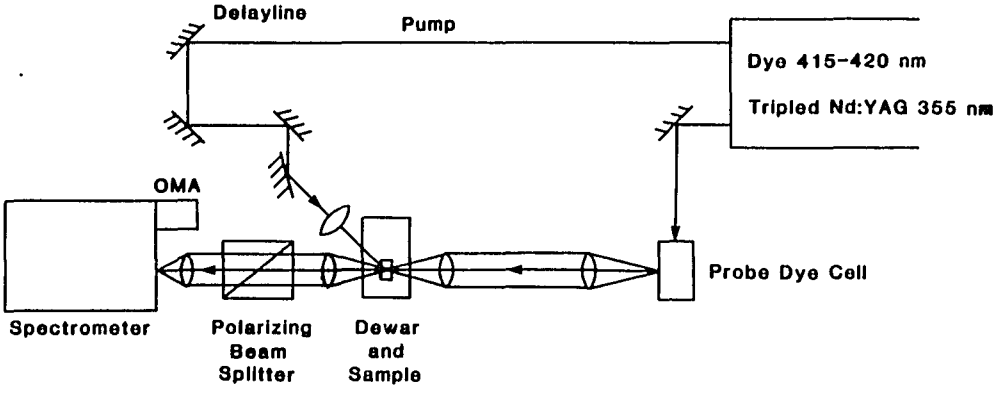

Fig. 4.1 Experimental setup for nanosecond time scale DTS measurements.

train, with a 5 ns tunable dye laser pulse. Temporal pulse overlap could be achieved with the pump optical delay line. Data was gathered by interleaved OMA integrations of the probe with pump on and off. The pump and probe pulses are shown in figure 4.2. The OMA detector was gated on for 5 ns centered on the pump pulse.

Results for several different CdS samples at different temperatures are shown in figure 4.3. CdTe spectra, for regions above the band edge, are shown in figure 4.4. The CdS bulk sample (crystallite radius must be at least several times the bulk exciton radius) behaved as expected; carriers are generated above the band, relax to the band edge, where they fill states and radiatively recombine. The quantum confined samples showed typical DTS for quantum dots. A large decreased absorption feature appears between the pump wavelength and the 1s-1s absorption feature, and smaller increasing and decreasing absorption features continue toward higher energies. A small increasing absorption feature is also apparent at low energy. There is little or no power broadening. The CdTe DTS is also consistent with differential spectra observed using cw excitation, as described presently.

The DTS was significantly changed by photo exposure. As shown in figure 4.5 the DTS spectrum decreases in magnitude and shifts to lower energy with increasing exposure. The first increasing absorption feature also increases with respect to the increased transmission feature. There appears to be an asymptotic limit to the DTS change after very large exposure. When the samples were at liquid helium temperature the photodarkening was significantly reduced, so that long term DTS data taking could be performed with no concern of the effect, except for the initial few pump pulses. These first pump pulses, with sufficient energy density, could saturate the sample 1s-1s absorption almost entirely, but the DTS quickly reached a steady state value below this. Photodarkening is drastically increased using high peak flux density excitation, and it

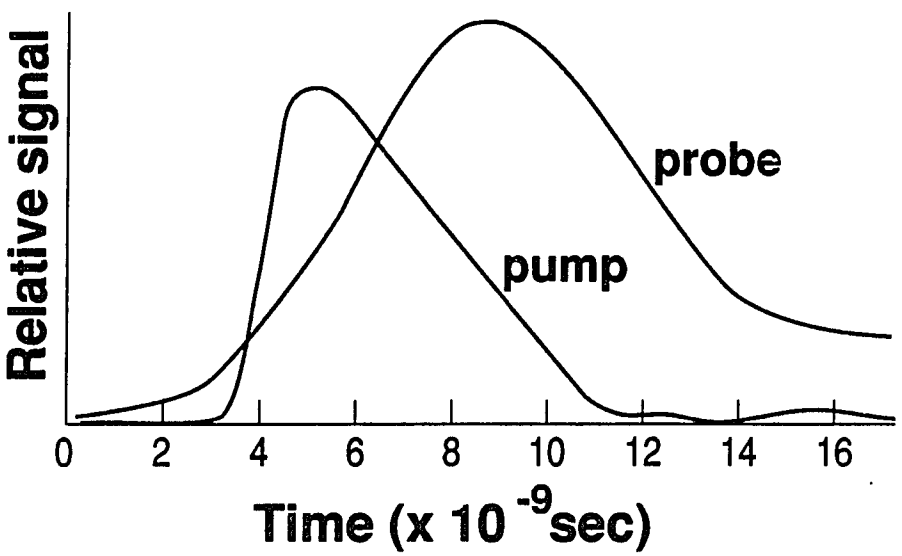

Fig. 4.2 Pump and probe temporal overlap.

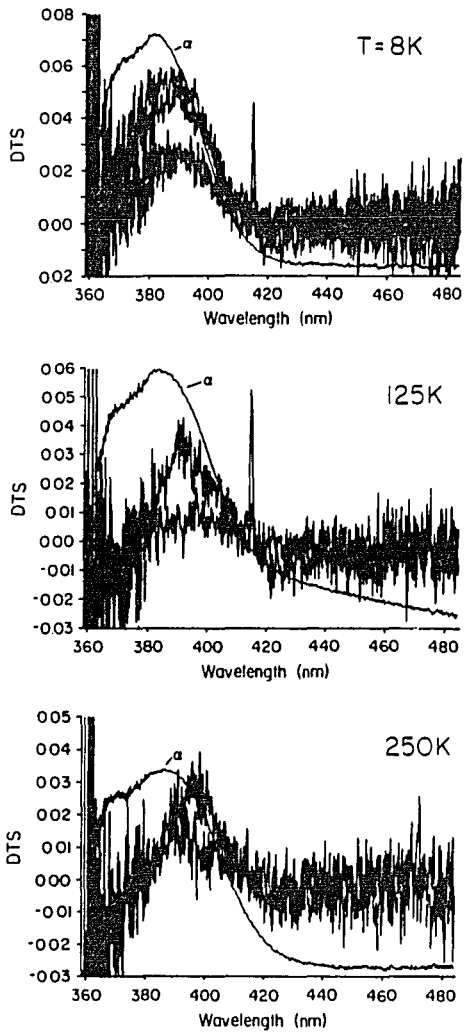

Fig. 4.3 A DTS for CdS sample 590-140, at various temperatures: pump fluences of 9.97, 4.50, 1.77, and .76 MW/cm^2.

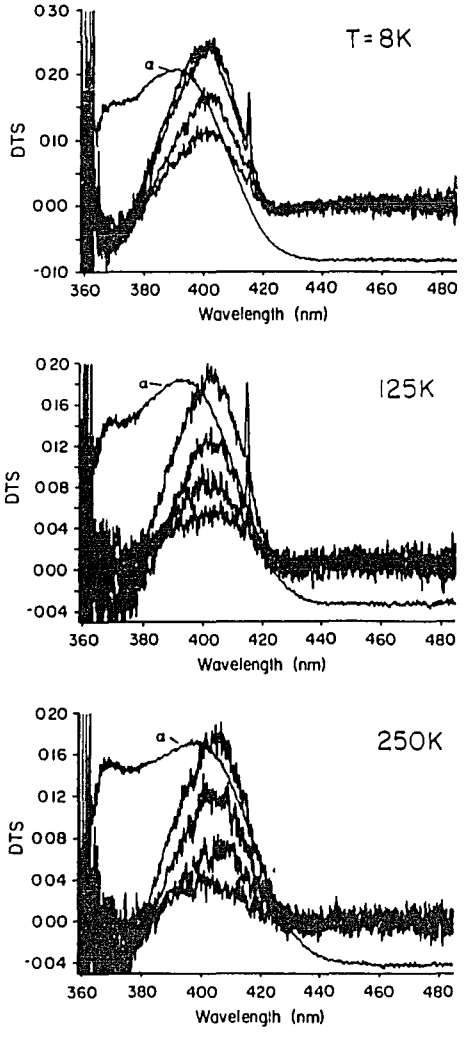

Fig. 4.3 B DTS for CdS sample 640-4, at various temperatures: pump fluences of 9.97, 4.50, 1.77, and .76 MW/cm^2.

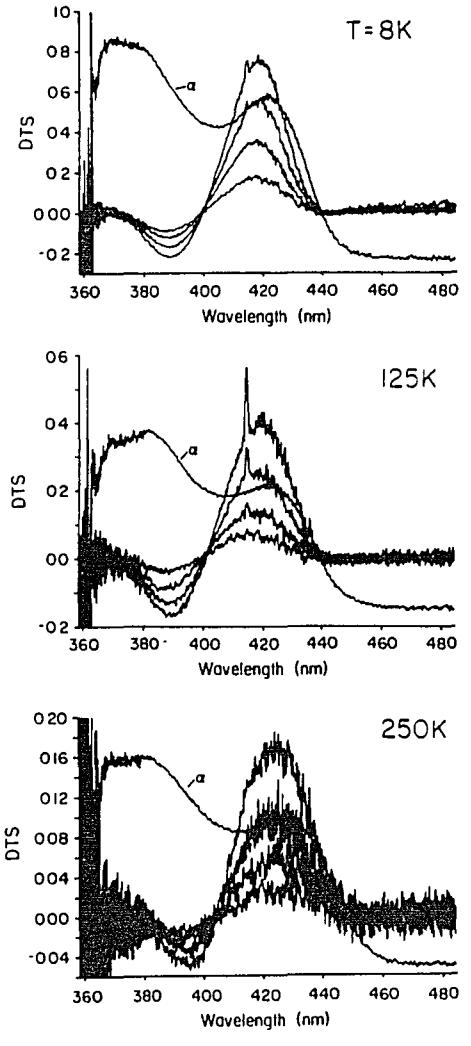

Fig. 4.3 C DTS for CdS sample 670-.25, at various temperatures: pump fluences of 9.97, 4.50, 1.77, and .76 MW/cm^2.

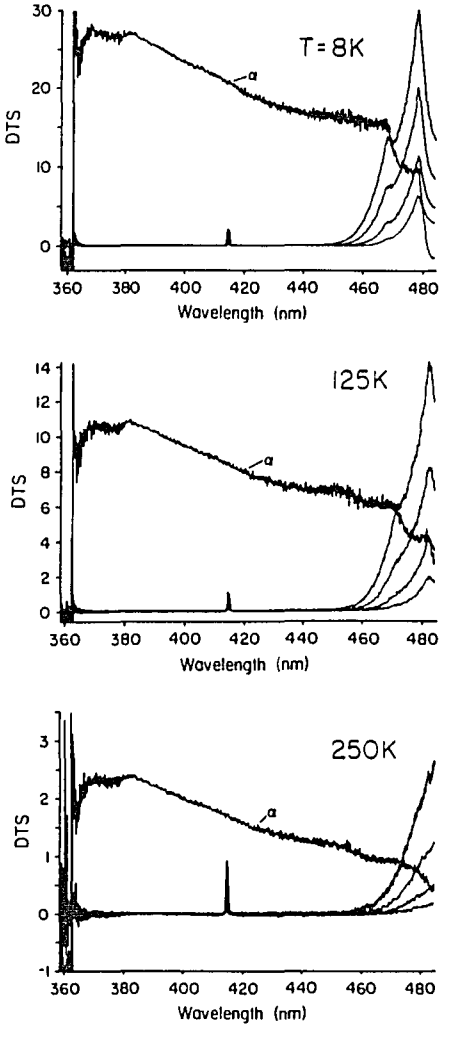

Fig. 4.3 D DTS for CdS sample 700-1, at various temperatures: pump fluences of 9.97, 4.50, 1.77, and .76 MW/cm^2.

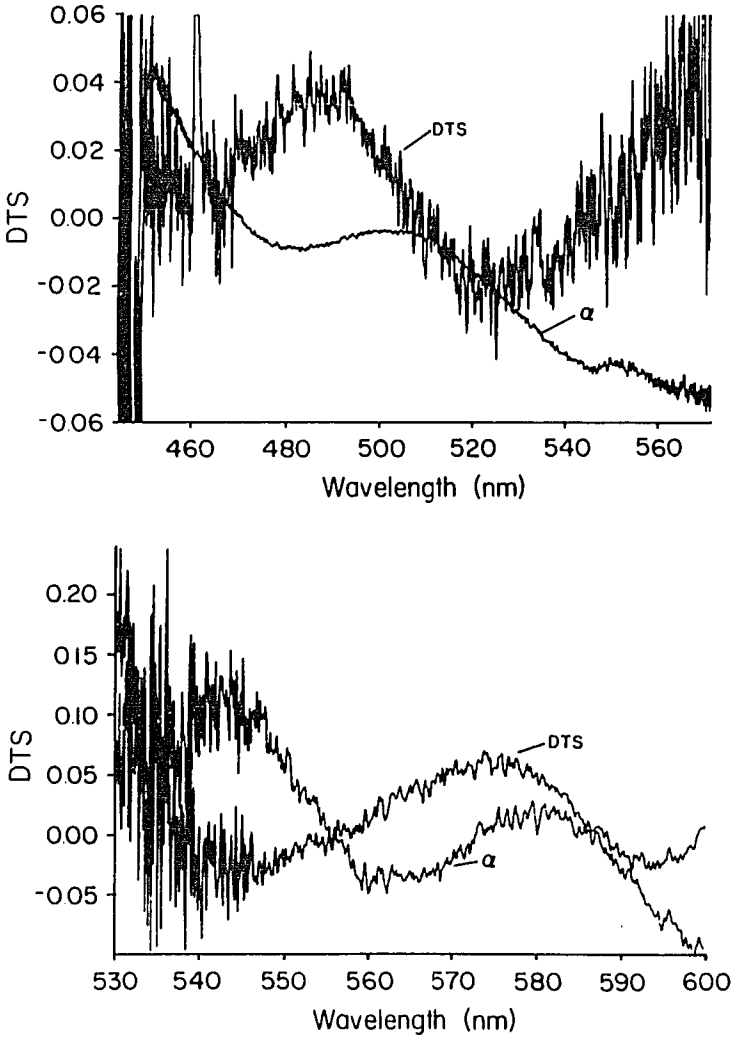

Fig. 4.4 DTS for CdTe, in regions above the 1s-1s transition.

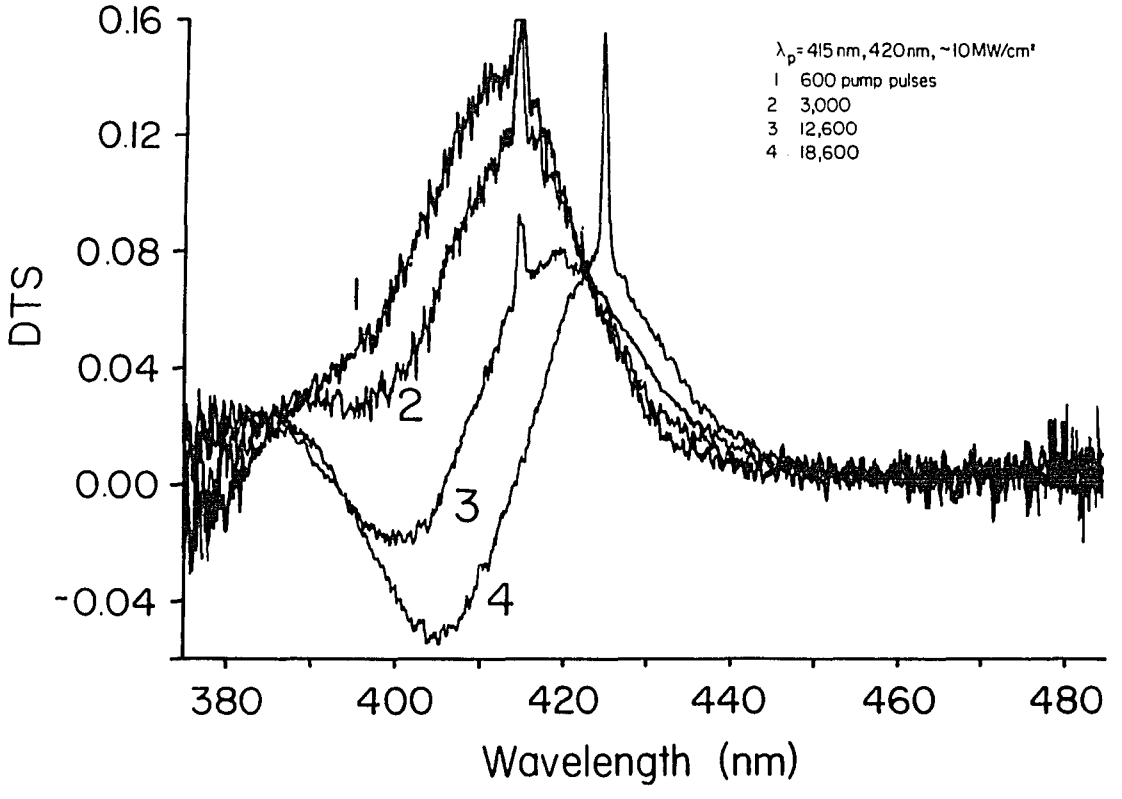

Fig. 4.5 Photodarkening effect for increasing exposure (α peak at 404 nm).

cannot be eliminated by using very low flux density excitation, although the photodarkening rate becomes very slow (several cw hours for obvious effects using $\simeq$10 kW/cm^2). It is notable that the permanent change of the linear absorption, as shown in figure 4.6, is similar to the initial non-photodarkened DTS, except the increased absorption feature at low energy is larger for the permanent case. Photodarkening can be removed by 48 hour heat treatment at 450°C.

It was noted that the DTS spectra were the same whether the detector was gated (sampling 5 ns of pump overlap with the >10 ns probe) or ungated (sampling during all of the probe duration). Using a delay line in the pump path, time-resolved DTS measurements were taken, with the resulting measured lifetimes of ~25 ns for CdTe and >30 ns for CdS. These lifetimes were quite inexplicable with respect to the anticipated carrier lifetimes in the discrete quantum confined levels. Additionally, in the case of CdTe the fluorescence lifetime was the same as that of the DAS. This suggested a correlation between the fluorescence and the differential absorption.

CW Differential Absorption

The basic experimental setup for the cw experiment is shown in figure 4.7 . The sample was probed with light from a Xenon lamp, filtered spatially and chromatically. A counter propogating tunable pump, of variable duration and period (the period adjusted to prevent thermal effects), was introduced via polarization, the spectrometer being further isolated by a second polarizer. The signal was obtained by two channel gated photon counting. The results, depicted in figure 4.8a (500 ns counting window within 1 μs pump pulse, pump wavelength 640 nm, pump peak power $\simeq$30 kW/cm^2), showed similar structure as that seen in the nanosecond excitation case, except the

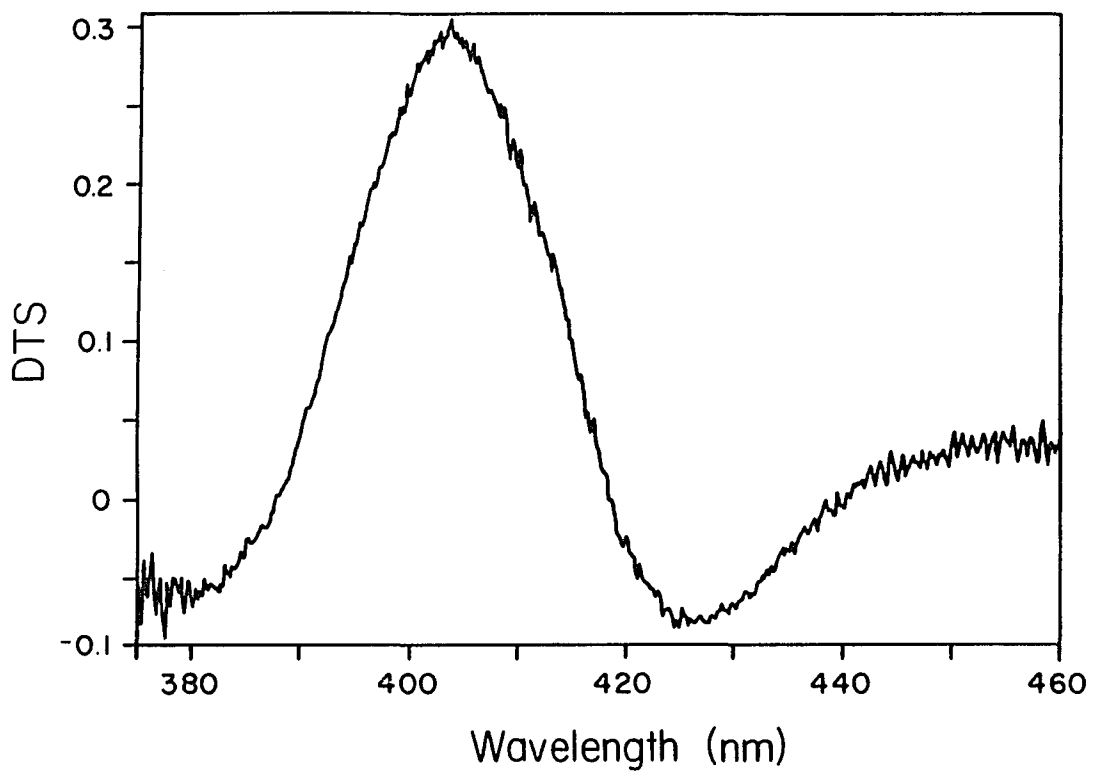

Fig. 4.6 Permanent change in the linear absorption, as expressed as a DTS, for sample of figure 4.5.

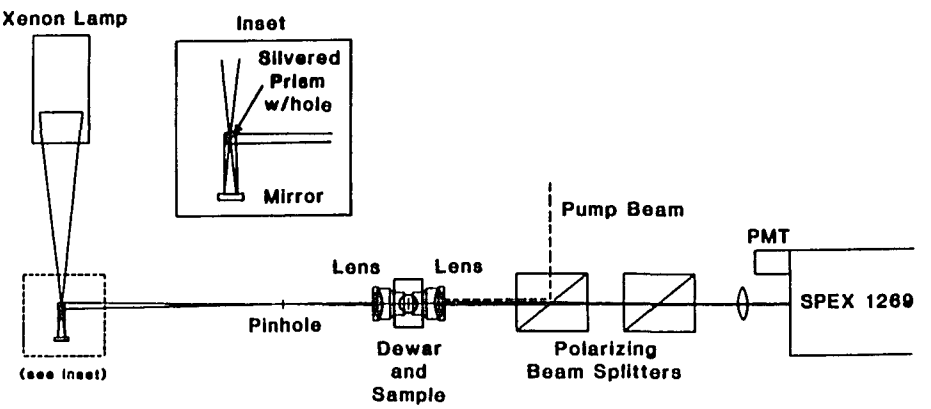

Fig. 4.7 Experimental setup for cw DAS measurements.

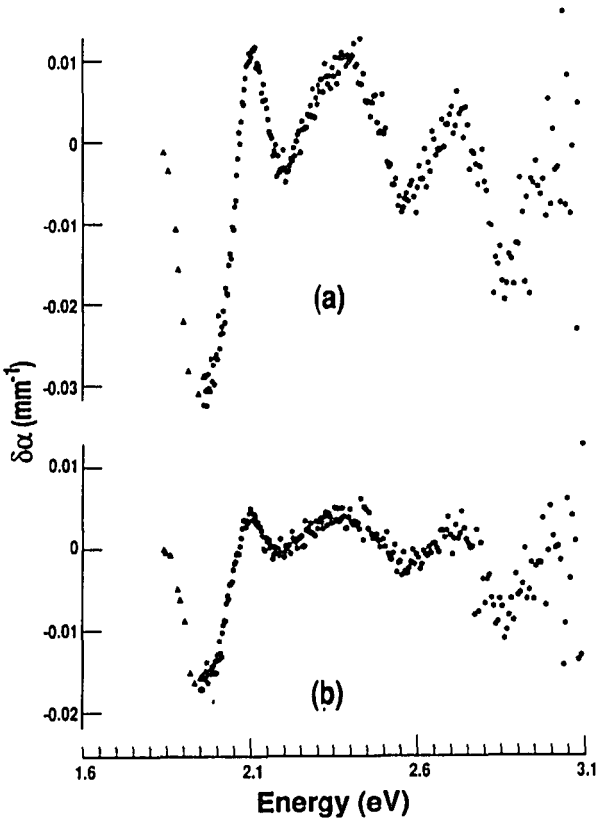

Fig. 4.8 DAS measurement on a CdTe sample: (a)500 ns within a 1 μs pump pulse, (b) DAS taken 1 μs after 1 μs pump pulse turned off.

entire absorption region could be observed. As in the nanosecond excitation case, a large decreased absorption peak was observed correlating to the 1s-1s absorption peak, and increasing and decreasing absorption features proceeded up the band. A large fluorescence feature was also encountered 60 meV below the pump excitation (figure 4.9). The fluorescence and DAS features shifted as one with the pump excitation, when the pump was within the 1s-1s transition. This is consistent with sampling a homogeneously broadened crystallite set within an inhomogeneously broadened feature due to a crystallite size distribution. This behavior was also observed using a 514.5 nm pump, although the magnitude of the DAS signal was reduced by 2 orders of magnitude for a given flux density.

The intense fluorescence caused complications in measuring the DAS because of the fluorescence's large magnitude with respect to the probe, and because of photodarkening that was always present to a certain extent, which made subsequent fluorescence subtraction impractical. Two methods were used to determine the signal in this region. First, a shutter was employed in the probe path so that background fluorescence could be measured at each point at the same time the differential signal was measured. Second, and more effectively, a laser probe was used to take data with essentially no fluorescence signal background, by virtue of the very intense spectral irradiance of the probe. This method produced the triangular points in figure 4.8.

The differential absorption was also taken with a 1 μs delay after the pump pulse was entirely off. The result, shown in figure 4.8b, demonstrates an exceptionally long lifetime for the differential signal. This seemed inconsistent with the lifetime observed when using nanosecond pump pulses, so an attempt was made to vary the pump duration while observing the decay of the differential absorption signal and the fluorescence. Figure 4.10 shows the DAS and fluorescence build up and decay, at fixed

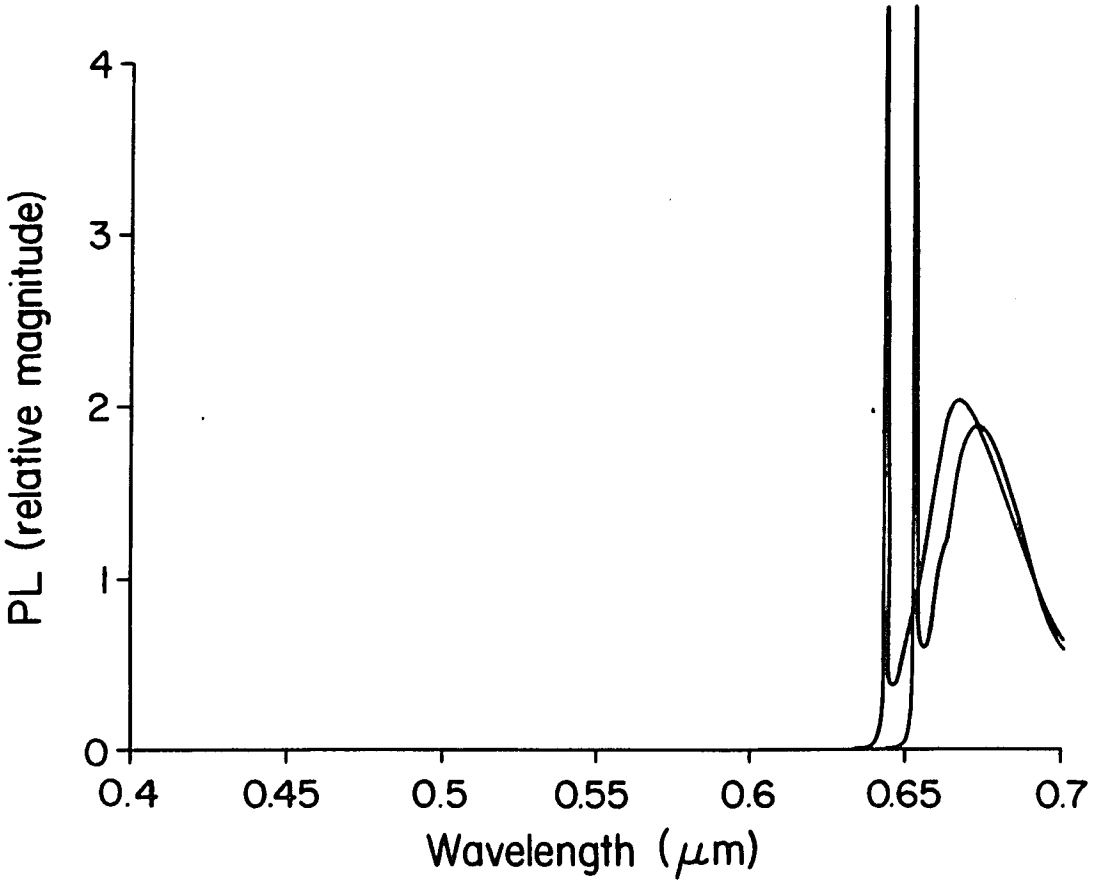

Fig. 4.9 Fluorescence signal for CdTe, during excitation pulse.

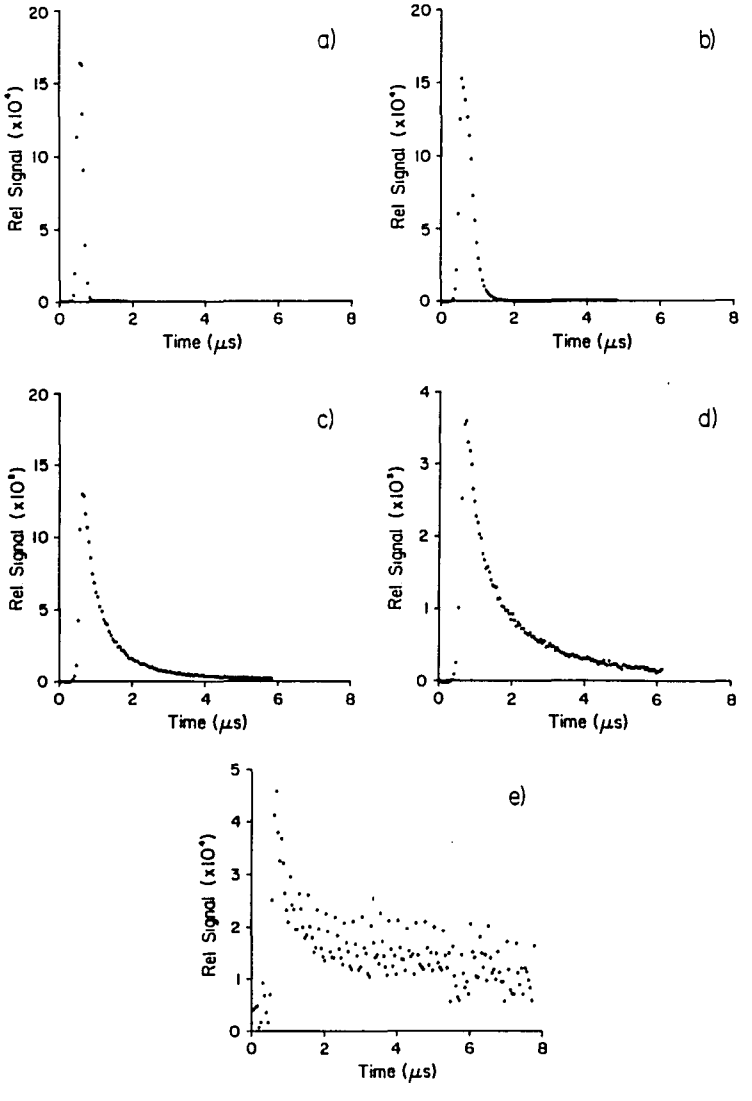

Fig. 4.10 A Fluorescence (PL) and DAS for 250 ns pump pulse: (a) pump, (b) PL 670 nm, (c) PL 780 nm, (d) PL 820nm, (e) Increased transmission at 640 nm.

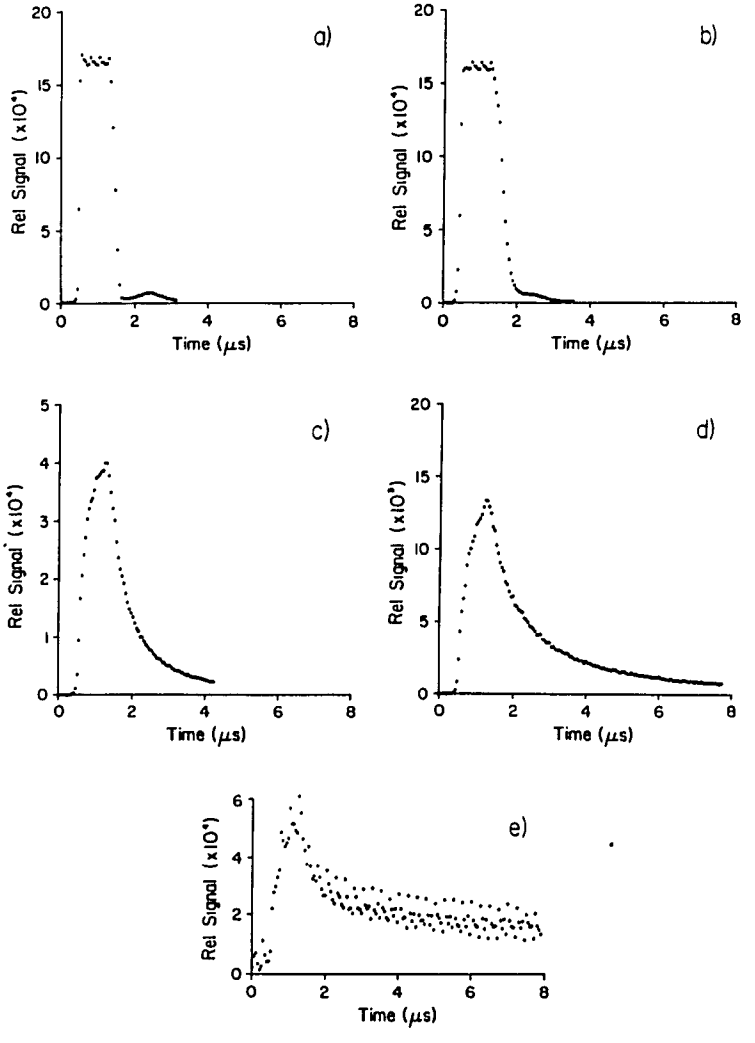

Fig. 4.10 B Fluorescence (PL) and DAS for 1 μs pump pulse: (a) pump, (b) PL 670 nm, (c) PL 780 nm, (d) PL 820nm, (e) Increased transmission at 640 nm.

wavelengths, for 250 ns and 1 μs pump durations. Figure 4.11 shows the differential increasing transmission at 635 nm with 4 μs and 10 μs pump pulses. Figure 4.12 presents the fluorescence spectra at various points in and after a 5 μs pump pulse.

The data seem to demonstrate at least a two component lifetime for the DAS, and a significant portion of the DAS signal has a lifetime too short to determine using the gated photon counting apparatus, and probably consistent with that measured with nanosecond excitation. The longer DAS lifetime of about 3 μs appears to correlate with deep traps, and the short lifetime (about 20 ns) with that fluorescence found 60 meV from the pump.

Clearly the initial carrier excitation is into the quantum confined levels, but lifetimes of 20 ns and greater are inexplicable for an electron-hole pair in a quantum dot in which increased overlap [Lee et al. (1986)] is expected to reduce the radiative lifetime, and surface interactions reduce the nonradiative lifetime. The 3 μs persistance is the same for 250 ns to 10 μs pump durations. The data appear to be evidence for the trapping (or escape) of one or both of the carriers, which reduces the electron hole overlap and thus the decay rate. The $\delta\alpha$ is maintained through the electric field (coulombic interaction) of the charges. The initial $\delta\alpha$, caused by the effect of the first electron-hole pair on the creation of the second, may not be discernibly different from the $\delta\alpha$ from the electric field; such is the case for a uniform field and nonlinear-optical $\delta\alpha$ for quantum wells [Miller et al. (1985), Chemla et al. (1985)]. Later, the charges must be seperated to explain the long lifetime. The similarity of the two effects is not surprising because both effects tend to wash out the quantum confined transition features, and because the coulombic interaction of an electron-hole pair is probably similar to one trapped and one free charge.

A possible origin for the higher energy fluorescence is the Cd^{++} vacancy, which

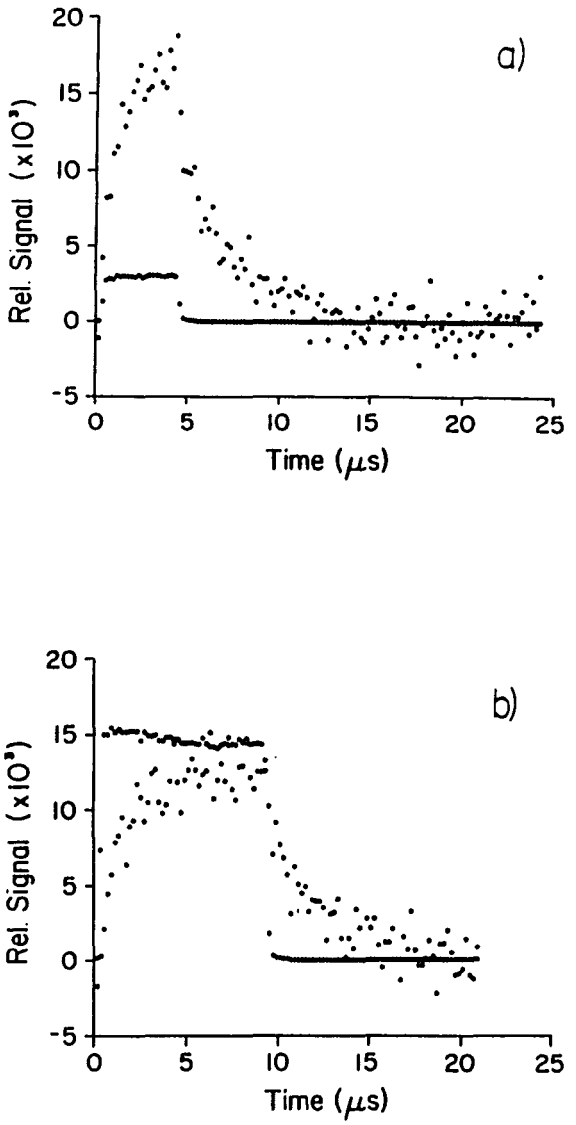

Fig. 4.11 Differential increased transmission at 635 nm for: (a) 4 μs pump, (b) 10 μs pump.

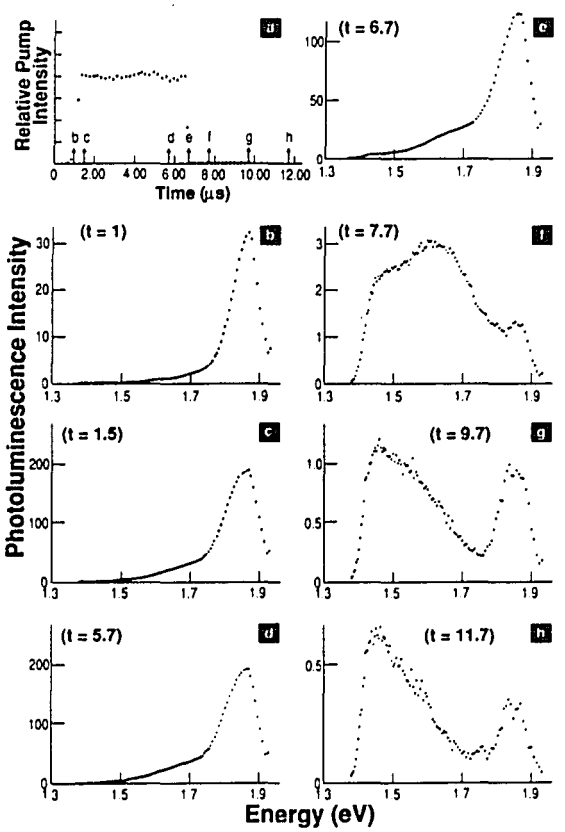

Fig. 4.12 Fluorescence for different times with respect to a 5 μs pump pulse.

is bound 60 meV below the conduction band of bulk CdTe [Madelung et al. (1987)] If a Cd^{++} captures an electron it would still have a net positive charge, and would repel the hole, and this would reduce electron-hole overlap. Calculations of a point charge configuration such as this, as described in chapter 3, show that a $\delta\alpha$ can result which matches the $\delta\alpha$ observed. The model used, however, is too simple to draw conclusions, and the particulars about the exact microscopic situation are unavailable anyway. The longer lifetime component of the $\delta\alpha$ must come from longer lived traps, such as those evidenced by lower energy fluorescence. By allowing a branching ratio from the 1s electron state to the trap states which strongly favors the higher energy-shorter lifetime traps, the behavior of the $\delta\alpha$ with different pump durations can be explained. It simply takes more excitation cycles (longer pump durations) to appreciably populate the long lifetime traps. By assigning 20 ns (high energy trap) and 3 μs (low energy trap) to the different trap states the $\delta\alpha$ behavior appears to be consistent. By the preceding arguements photodarkening can be attributed to trapping by deep, very long lifetime trap states.

CHAPTER V

AN OPTICAL ASSOCIATIVE MEMORY

The preceding chapters described the linear and nonlinear behavior of a quantum confined material system. Those investigations were motivated in part by the desire to find a 'better' nonlinear material to employ in a nonlinear device, which in turn might be used in an optical processor of some description (possibly a signal processor or computational system). The all-optical system described in this section demonstrates the use of nonlinear devices to make decisions. In this associative-memory system, conventional optical techniques play the key processing role through matched filtering of a partial input. The nonlinear optical decision-making element utilizes the output of a holographic matched filter, the cross-correlation beams, to determine the closest match. The corresponding hologram then is read with a counterpropagating beam.

Motivation and Concept

Experiments that demonstrate the use of optics with optical nonlinear devices [Gibbs (1985)] for optical computing have served primarily to demonstrate the weaknesses of optics in comparison to electronics when competing in like applications. An example, described in reference [Wang et al (1988)], illustrates the use of ZnS interference filters as nonlinear decision-making elements in a system which employs cascading, and a moderate amount of parallelism, to recognize simple three spot patterns

in an input spot array. The experiment also illustrates the difficulties of dividing a beam into many beams so that each decision-making pixel receives the same amount of power in approximately the same cross sectional area. These geometrical optics difficulties and the high power requirements of large arrays of nonlinear decision-making pixels are formidable hurdles in the realization of massively parallel optical computing systems. This suggests that the best application of nonlinear decision-making may not be in numerical computing, which is already accomplished easily with electronics. Rather, the best application may be to combine more traditional optical techniques of image processing, for example, real-time correlations, with a limited amount of nonlinear decision-making. Only if several correlation peaks or other events occur simultaneously will the system activate an appropriate response. An example of such an application is the associative memory.

An associative memory can be defined as a memory in which a stored piece of information can be retrieved as a whole when a probing input is only partially complete or even distorted. Memory and thresholding functions are two essential ingredients to the associative memory, and the main advantage that optics offers is the capacity to provide the massive parallelism required for global interconnections. A Fourier hologram can be used to memorize or store a set of images, and the available recording materials range from emulsion-based to crystal-based materials. Decision-making feedback can be provided by the thresholding function of nonlinear devices such as ZnS or ZnSe IFs, GaAs etalons or photorefractive crystals.

Recent work involving associative memories based on various thresholding and feedback schemes [Hopfield (1982), Kohonen (1984)], and several optical implementations have been demonstrated [Psaltis, Farhat (1985), Abu-Mostafa, Psaltis (1987), Paek, Psaltis (1987), Anderson, Erie (1987)]. The optical associative memory

discussed here, which is similar to that presented by Soffer, et al., decides which stored object most closely matches a partial-object input [Owechko (1987)]. The associative memory employs two elements. The first element, a Van der Lugt correlator, gives an analog 'degree-of-match' value, and the second, an optically bistable interference filter, gives a binary thresholding response.

The idealized system works by writing Fourier transform phase holograms, sequentially multiplexed in reference beam angle, of the different objects. The test object then is correlated with the stored objects, giving angularly separated cross-correlation beams. Each beam is focused onto an optically bistable IF where the decision of closest match is made at the central peak positions.

ZnS interference filters, grown in the Thin Films Coating laboratory at the University of Arizona, were used as nonlinear decision-making devices. With appropriate optical biasing and configuration the devices may be used to perform a variety of logical functions. The devices have millisecond recovery times; they operate in the visible, facilitating alignment; and they are relatively easy to grow or inexpensive to buy. These characteristics make them attractive for demonstrating optical computing concepts. However, their lack of uniformity and long term stability make it necessary to search for good regions repeatedly. The particular interference filter used had the structure $G(HL)^{5}2H(LH)^{5}G$, with a linear transmission of 54% at $\lambda = 513$ nm; FWHM = 15 Å; and minimum switching power of 22 mW. The interference filter was used in conjunction with a holding beam in this experiment. Power is supplied, in this case exactly counterpropagating with each correlation beam, in order to bias the device very close to the switching threshold. Only the minimum switching power then is necessary to push the device into the transmissive mode. This process reduces the required correlation power and thus the power through the hologram. The

counterpropagating bias beam also facilitates the recall of stored objects.

One of the beams, corresponding to the most closely matched stored object, is sufficiently intense to provide the minimum switching power, allowing the holding beam to colinearly counterpropagate to the hologram. Because this beam is a plane wave at the proper incident angle to the hologram, it reads the appropriate object from the hologram, and the object is propagated back through the optical system. Also, because the hologram is thick, only this object is Bragg matched; no other objects are read out. This overall process is the auto-associative mode of operation. A partial object input recalls a reconstruction of the same object.

If the holding beam is propagated to another hologram or transparency a hetero-associative recall can also be performed. In this case any output can be associated with a matched partial input.

Experimental Apparatus

The experimental setup is shown in Fig. 5.1. In the recording stage, a collimated beam (the object beam) illuminates a transmissive object, a black-ink fingerprint on a slide. The object beam is transformed by a lens onto the Fourier plane where a holographic grating is formed by interfering with a collimated reference beam in dichromated gelatin (DCG). Two separate objects, labeled F2 and F3 (Fig. 5.2), were used in the experiment. F2 was interfered with a reference beam angle of 47° at the Fourier plane, and F3 was interfered with a reference beam angle of 58°.

Volume holograms have been shown to be better than the thin hologram in the application of matched filtering, resulting in better SNR, increased brightness of the correlation peak, and better spatial separation of the output signal. DCG, one of the

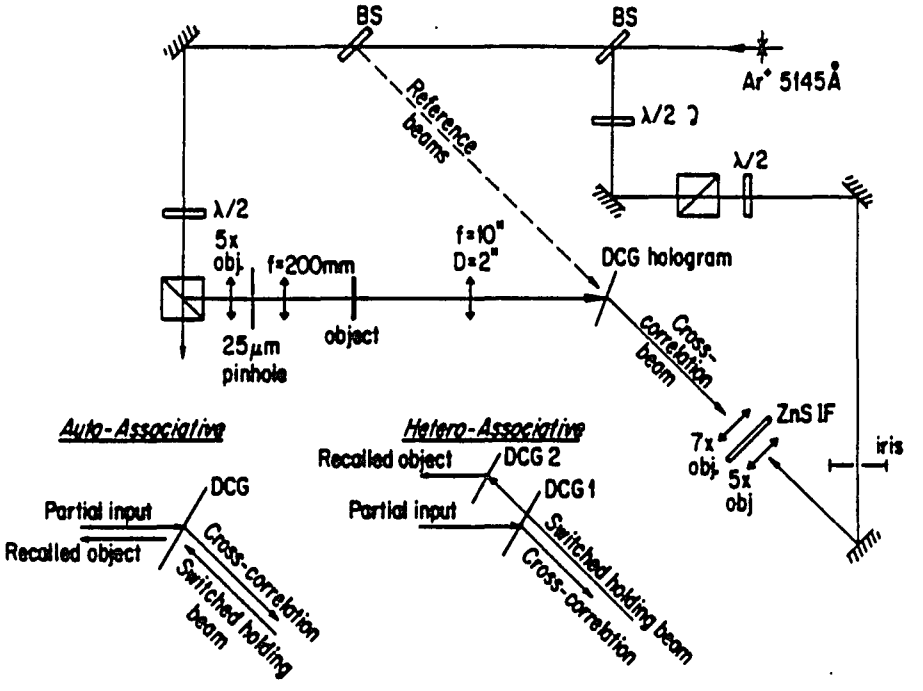

Fig. 5.1 Experimental arrangement for associative memory.

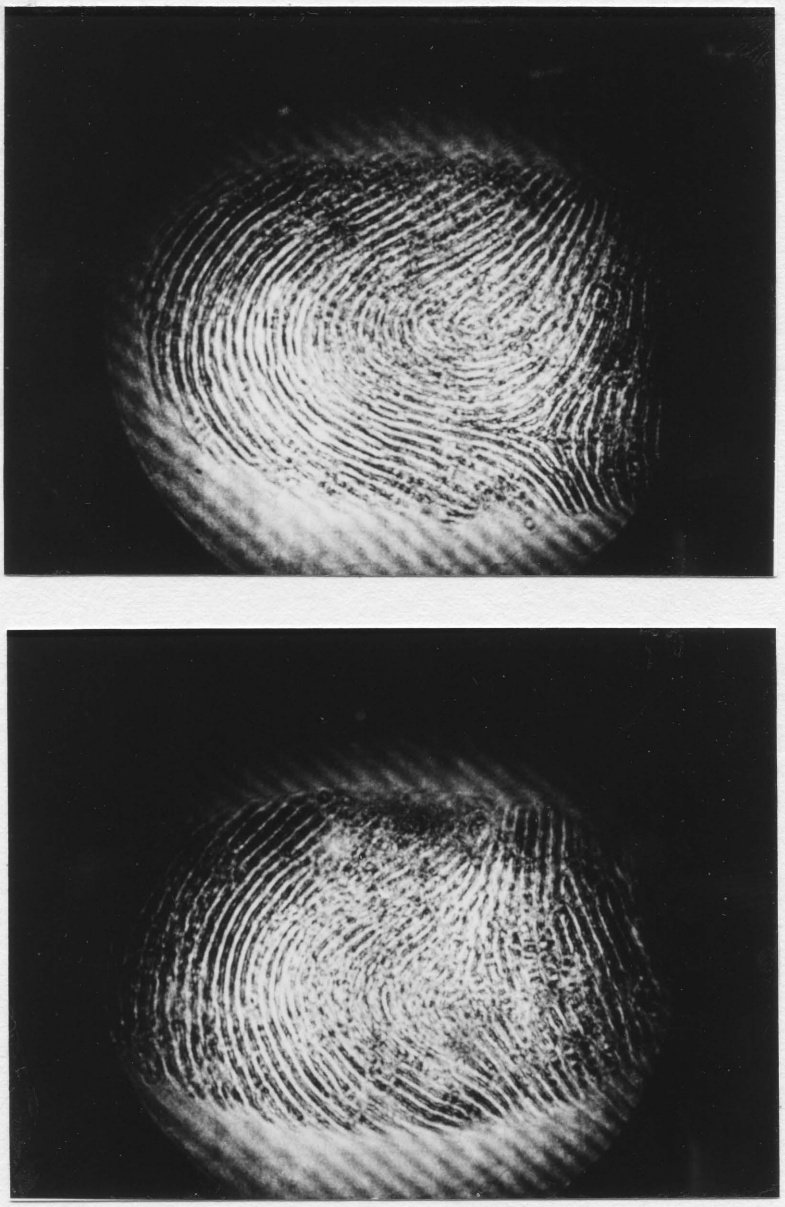

Fig. 5.2 Object fingerprints: top; F2, bottom; F3.

volume hologram materials, is a near-optimum hologram recording material, but it requires tedious processing. A considerable effort was made to optimize the DCG hologram [Geogekutty, Liu (1987)].

The system require optimal discrimination to permit a minimal partial-object input. Switching power constraints for the optically bistable IF dictated some minimum auto-correlation efficiency. These requirements lead to a trade-off between system efficiency and discrimination. The object fingerprints, consisting of parallel curved ridges of roughly equal spacing, had a fairly low modulation depth, thus only 20% of the power was in the diffracted "information ring" of the Fourier transform (Fig. 5.3). In addition, the relative intensities of the Fourier transform information showed a large dynamic range, from 1:15 to 1:500 compared to the zero-order. Such a large dynamic range generally cannot be accommodated by a recording film. This problem may be treated in two manners. First, one may wish to operate away from the Fourier plane, at a plane where the light distribution is more homogeneous. This should imply less object discrimination and less immunity to shift, scale and rotation. Second, one may wish to encode the object on a homogeneous spatial frequency "background," for example, a Lambertion plate. This method produces high discrimination due to the Lambertion alone and also has very poor scale, shift and rotation behavior.

Using carefully controlled objects, where the distinctive properties of the object will produce standard intensity Fourier transforms, diffraction efficiencies greater than 90% may be obtained. This efficiency degrades rapidly with the number of stored objects, depending on the method employed to store the holograms. The phase dynamic range of the holographic media is limited.

It was important to determine the appropriate reference/object beam ratio to give optimal grating visibility for the best efficiency while maintaining sufficient

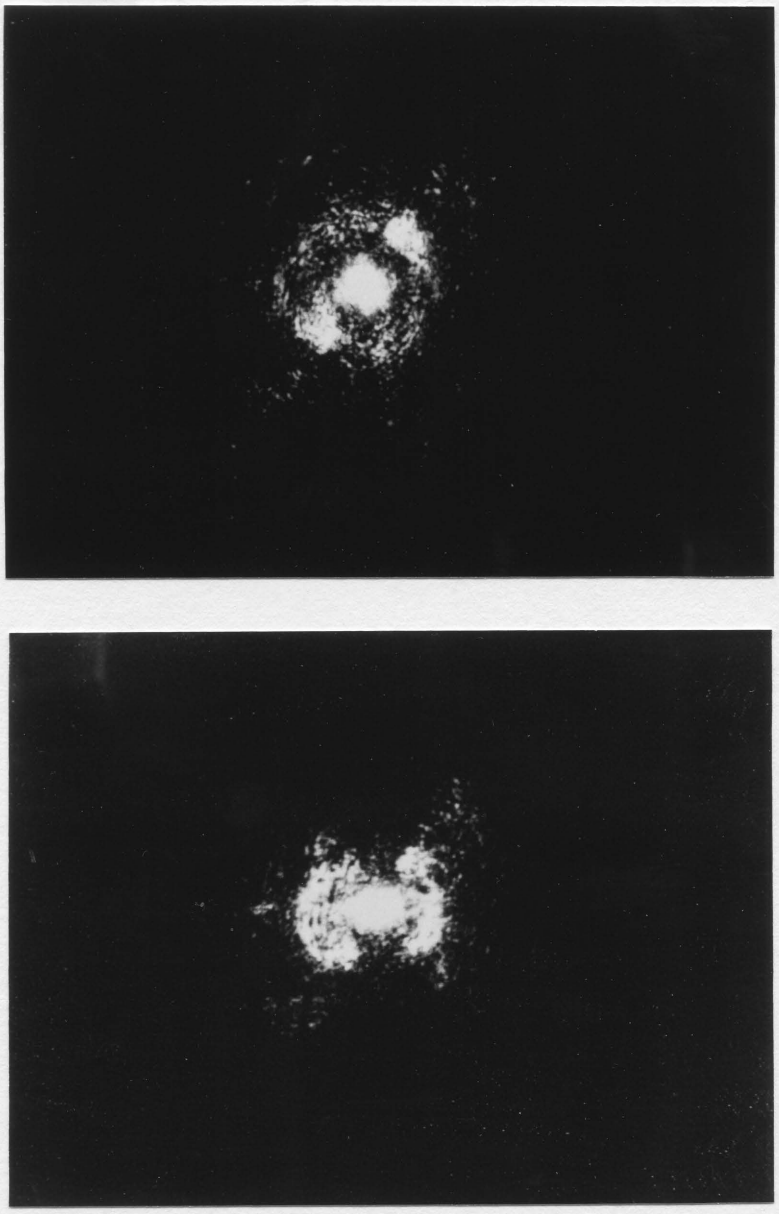

Fig. 5.3 Photograph of the Fourier transform plane for the object fingerprints: top; Fourier transform plane for F2, bottom; Fourier transform plane for fingerprint F3.

discrimination. It was also critical to ensure that the zero-order saturated the DCG, so that the holographic fringes are suppressed. This step eliminates the contribution to cross-correlation attributed to the zero order. Even when the zero-order saturates the DCG, some unwanted modulation occurs in the wings of the feature. Large diffraction from the zero-order would destroy the discrimination, because all objects have similar zero-orders. It was found that a reference-to-object ratio of 1:20 in the Fourier transform plane (taking the peak of the zero-order as the object intensity) and about 190 mJ/cm^2 exposure gave 4% auto-correlation efficiency; this maximized the efficiency-discrimination trade-off in this experiment.

Results

During operation of the system, one of the objects was partially obstructed and illuminated (Fig. 5.4), causing auto-correlation beams to be diffracted from the hologram at the two reference angles. The autocorrelation peaks can be seen for F2 and F3 in Fig. 5.5, for the unobstructed and partial cases. For a partial input, the discrimination ratios (auto-correlation intensity versus cross-correlation intensity, in the correlation plane) of the correlation peaks were 50:1 with F2 as test object and 10:1 with F3. The reduced discrimination for partial F3 input was attributed to its smaller modulation depth, resulting in a larger zero-order content.

The auto-correlation peak for the partial-object input was of sufficient intensity (about 3 mW in a 100-μm-diameter spot) to switch the optically bistable IF into the transmissive mode with a 20 mW holding beam (Fig. 5.6). Switching of the optically bistable IF allowed the counter-propagating holding beam to read out the hologram. The auto-associatively reconstructed image from a single readout beam (Fig. 5.7(a)) had

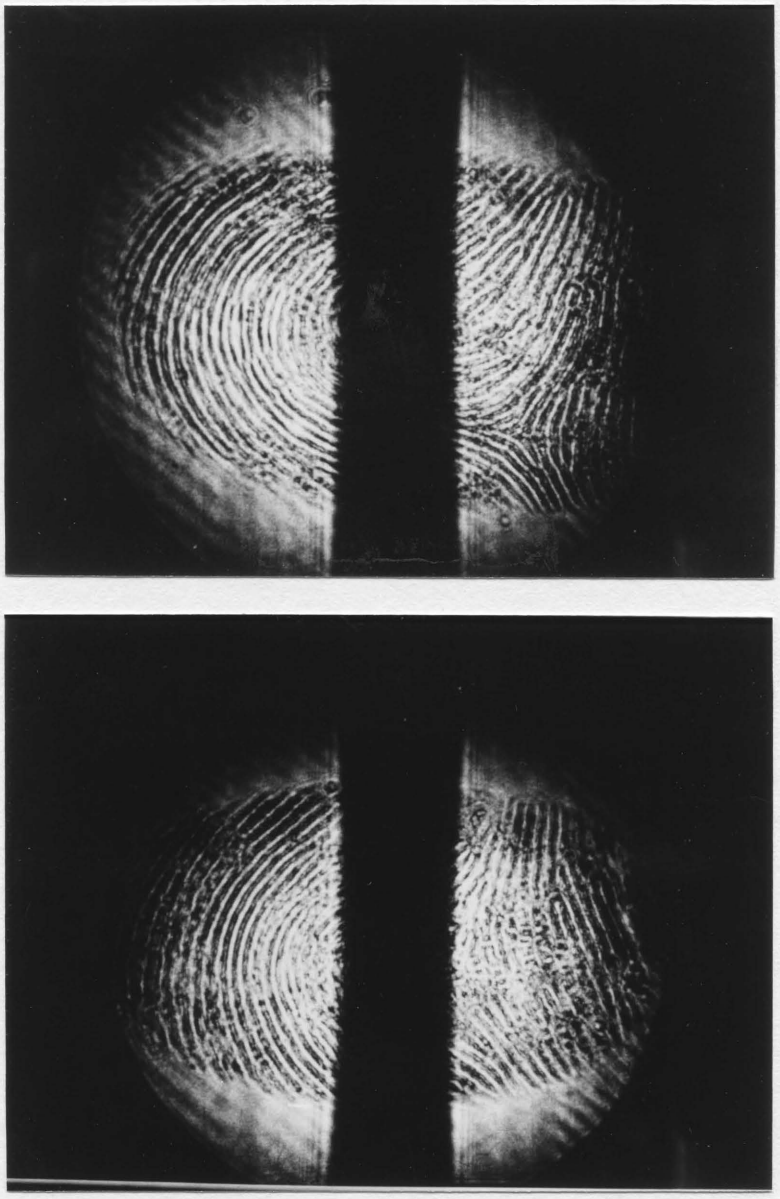

Fig. 5.4 Partially obstructed objects: top; F2, bottom; F3.

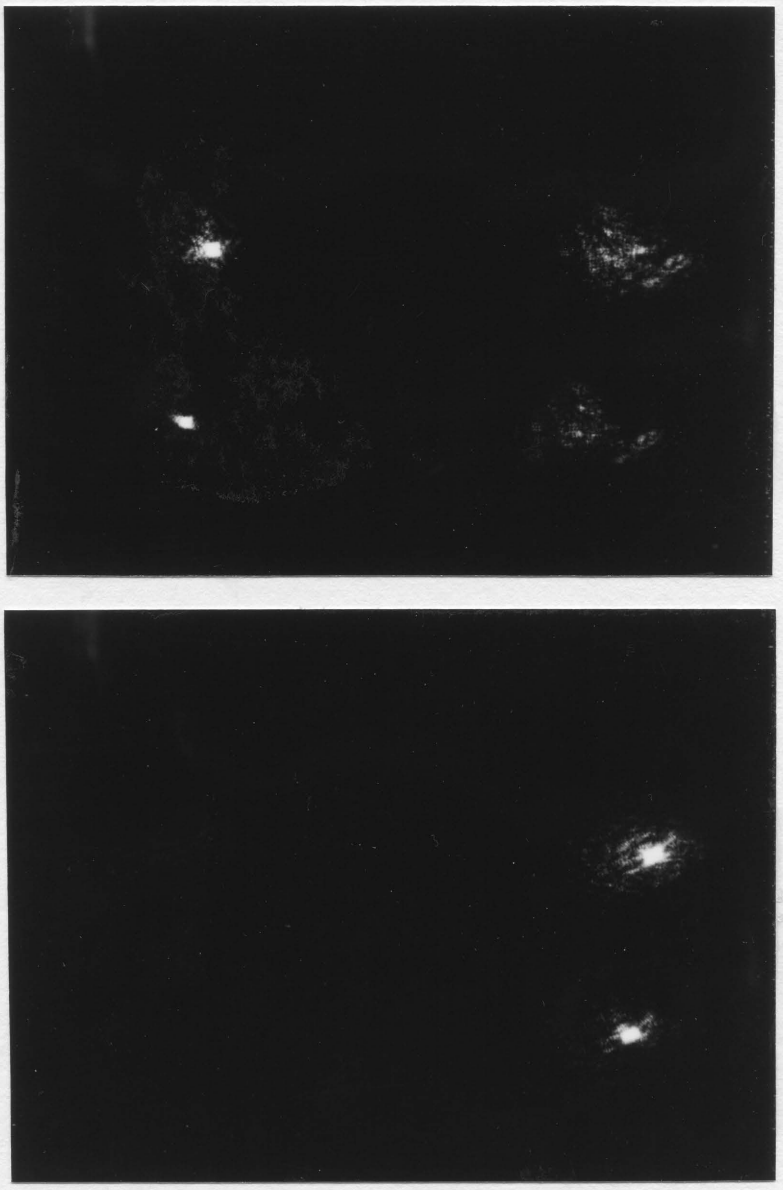

Fig. 5.5 Cross-correlation beams for partial and whole input objects. Top: Upper; partial F2 input, Lower; whole F2 input. Bottom: Upper; partial F3 input, Lower; whole F3 input.

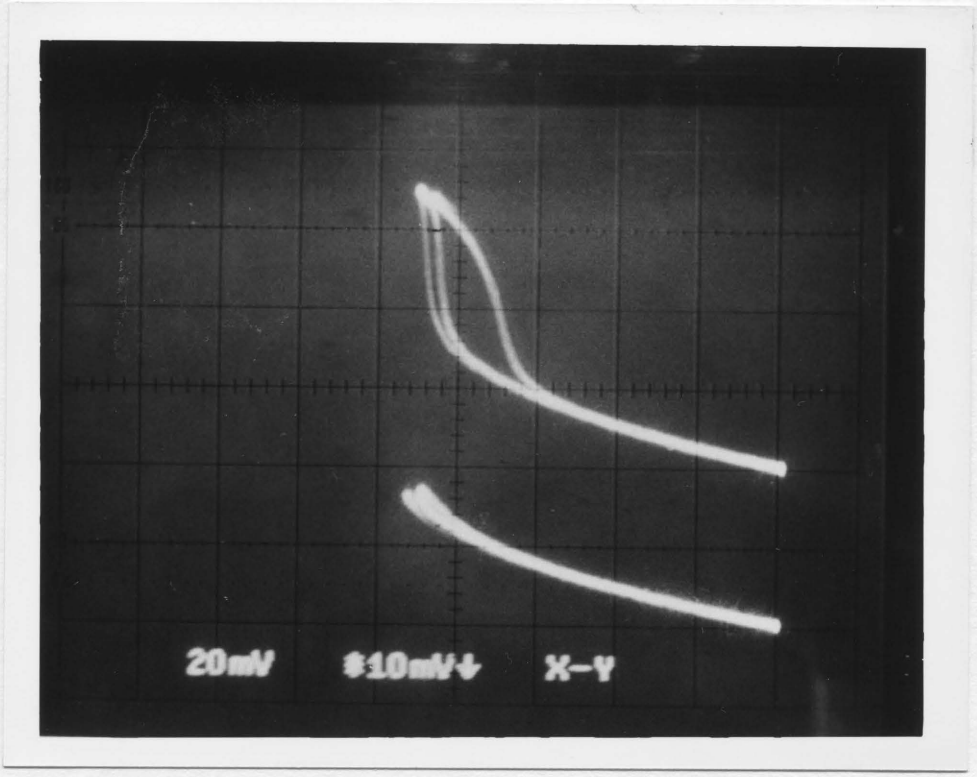

Fig. 5.6 Optically bistable IF response: Upper, switched on by the correlation input (vertically off-set for clarity), Lower; switched off. (Trace describes input holding-beam intensity, -x, versus transmitted holding-beam intensity, y).

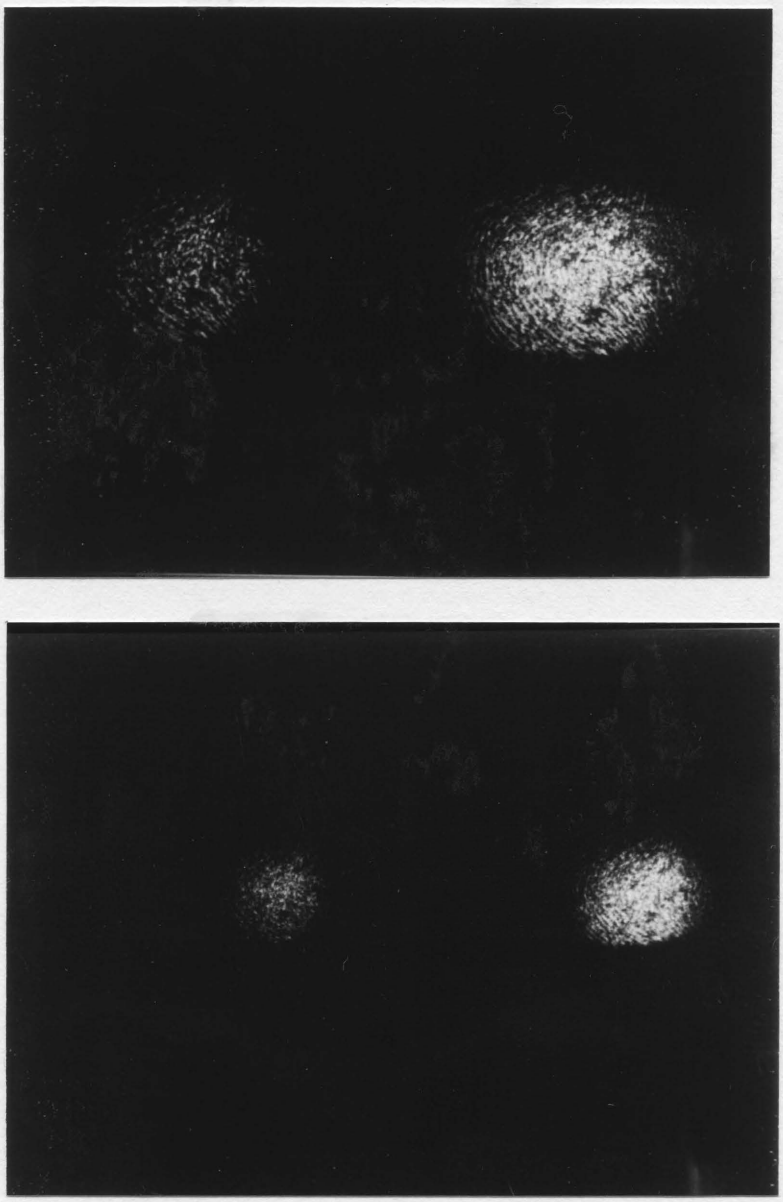

Fig. 5.7 Recalled object F2. Top: Auto-associatively recalled: Left; switched off, Right; switched on. Bottom: Hetero-associatively recalled; Left; switched off, Right; switched on.

a contrast ratio of 2:1 (the ratio of the switched holding beam transmission to the passive optically bistable interference filter transmission of the beam, or equivalently, the switching contrast of the optically bistable interference filter). The hetero-associative reconstruction yielded similar results, as seen in Fig. 5.7(b). Because the diffraction efficiency of the hologram was only 4%, at least 75 mW of object input beam power was required, causing dynamic thermal damage in the DCG. The poor quality of the reconstructed objects was attributed to this thermal damage.

Decision-making was demonstrated on only one cross-correlation beam at a time, having determined that sufficient discrimination was present to preclude simultaneous switching of the beams. However, if two devices had been installed each would have produced an off-state recall (from the off-state linear transmission of the holding beam through the IF), further degrading the on-state recall discernibility.

In a previous experiment one object was stored, the letters "WX," a partial input, was recognized, and associative recall was executed (Fig. 5.8). In this case discrimination was not necessary (only one object was stored) so that increased cross-correlation efficiency could be obtained through the use of the zero-order. High quality recall was facilitated because thermal damage was not an issue.

Summary and Discussion

An associative memory for fingerprint identification has been constructed using a Van der Lugt correlator and an IF as a thresholding device.

In the associative memory the DCG holographic Van der Lugt filter limited the performance of the system. Although the object employed was responsible for certain aspects of the experimental difficulty, even under ideal object conditions the diffraction

Fig. 5.8 Recognition of partial input for stored "WX." Top; partial input, Bottom left; recall switched off, Bottom right; recall switched on.

efficiency achievable will be a limiting factor. This problem is aggravated as the number of stored objects is increased [Hong, Psaltis (1986)]. Photorefractive materials may serve to increase the number of stored objects, by means of their large material thicknesses, but typically the diffraction efficiencies are even more limited than with DCG holograms. The power throughput requirements dictated by subsequent nonlinear devices can also introduce serious complications, becasue of the storage and erasure dynamics of photorefractive holograms. These dynamics can also introduce new flexibility to the holographic element.

Optical nonlinear devices were successfully employed as decision-making elements in these all-optical systems. However, the limiting aspects of the nonlinear devices and the holographic element were felt even in these comparatively simple systems.

APPENDIX A

PHOTON COUNTING

Photon counting techniques may be used to detect very low intensity signals. In addition, because photon statistics apply, signal-to-noise scales as $N^{1/2}$, and thus arbitrarily large signal-to-noise levels are achievable (however, arbitrarily long times may be involved). Photon counting techniques were used for one or both purposes in the previously described experiments. The practical application of photon counting, and the photomultiplier tubes that are used, is fairly straight forward, but not without pitfalls. Presented here is a short summary of photon counting and some practical application notes, more often than not, learned by trial and error.

Photon counting starts, of course, with the detection of photons. In this case a photon interacts with the photocathode of a photomultiplier tube (PMT) ejecting an electron. The electron is accelerated through a potential and strikes a dynode, ejecting typically 4 to 6 additional electrons. These electron are accelerated to a second dynode and the process repeats for up to typically twelve dynodes. In this manner electron gains of 10^6 are easily realized. The current pulse so generated is applied to an impedence and this voltage pulse, sometimes after further amplification, is presented to the photon counting electronics.

The photon counter is just a voltage discrimination circuit. Descriminators determine if the voltage pulse excedes a certain set value. In order to define a window of acceptable peak voltage two seperate counters, lower level (A) and upper level (B),

are used, the descrimination levels of which are selected to correspond to the voltage values expected for one photon voltage events. The number of counts in the window is then just the number of counts A minus the number of counts B.

The primary purpose of the counting discriminators is to eliminate noise signals that come from all PMTs. In addition to the photogenerated electrons already mentioned, thermally generated electrons are created at the photocathode and at each dynode. The dynode thermal electrons will generate a current pulse smaller than that of photocathode electrons, and hence these signals will be eliminated by the lower level discriminator. The photocathode thermal electrons are indistiguinsable from photoelectrons. The thermal emission rate from the photocathode, and from the dynodes, may be drastically reduced by cooling of the PMT (improvement is seen down to -50C). Other larger amplitude noise signals also occur (originating for example, from cosmic radiation) and these are eliminated by the upper level discriminator. The placement of the discriminator levels is facilitated by taking a pulse height distribution (PHD) curve shown in figure A.1 (scanning a narrow discrimination window over voltage values).

Practical Considerations

Photon Counting Electronics:

The count rate of the discriminators must not excede the level dictated by the limiting pulse pair resolution, either that of the electronics or that of the PMT, and photon statistics. Given that a photon has just been detected, the probability that a second event will occur within the limiting pulse pair resolution time t is

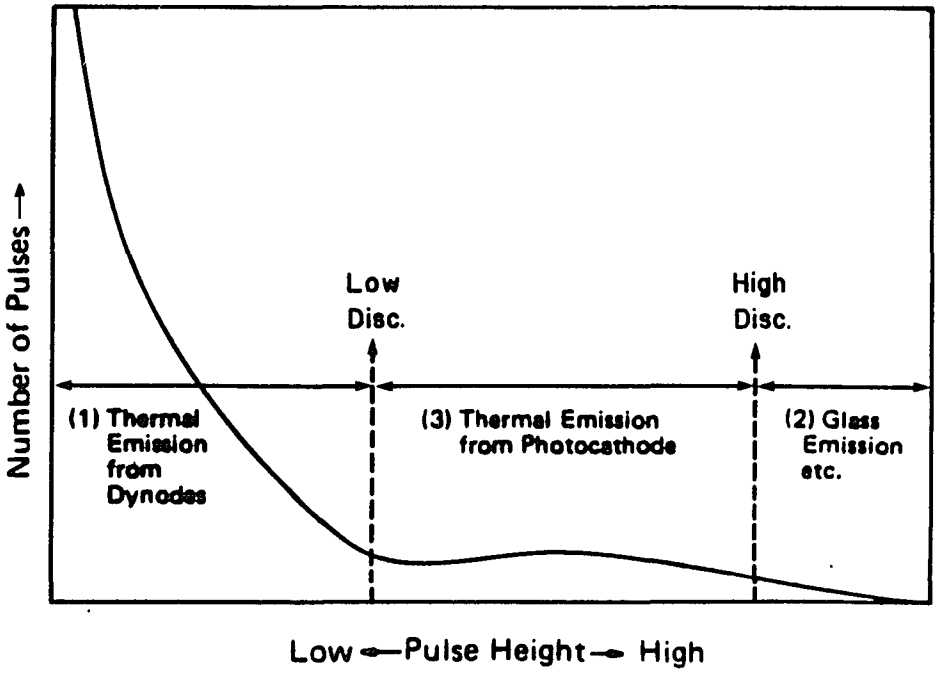

Fig. A.1 Pulse height distribution of noises.

$$P_t = \frac{[\nu t]^m}{m!} \exp(-\nu t)$$

where ν is the average rate of detectable events. The rate of undetected counts $P\nu$ must be much less than the count rate ν, and is of particular concern when measuring small signals over regions of wide count rate changes.

In many applications, such as the detection of differential signals in gated photon counting, the two (or more) discriminators are used as separate channels, instead of a lower and upper level for a single channel. In this case it is critical that the discriminators and gate widths are set to equal values, so that a true zero signal may be known. This must be corroborated by measurement over the entire counting dynamic range that will be experienced. In practice each counter channel is nonlinear and a good zero will be hard to achieve over several orders of magnitude.

Photomultipliers:

The selection of a photomultiplier depends on the application in which it will be employed. For low count rates, where the highest quantum efficiency and smallest dark count rate is necessary, a GaAs photocathode product (Hamamatsu 943-02, Burle (RCA) 31034), is desirable. For high count rate small signal detection applications where system stability is critical (as in the quantum confined Franz-Keldysh measurment) a tube with an optimized photon counting design, including a GaP first dynode, is required (Hamamatsu 1333, Burle 8852). The discriminator may be placed in the distinct valley of the 1333 PHD curve (figure A.2), and the count rate is relatively immune to voltage fluctuations that might translate into large variations for the 943-02 tube. When simultaneously using more than one PMT, for example, when an input and transmitted

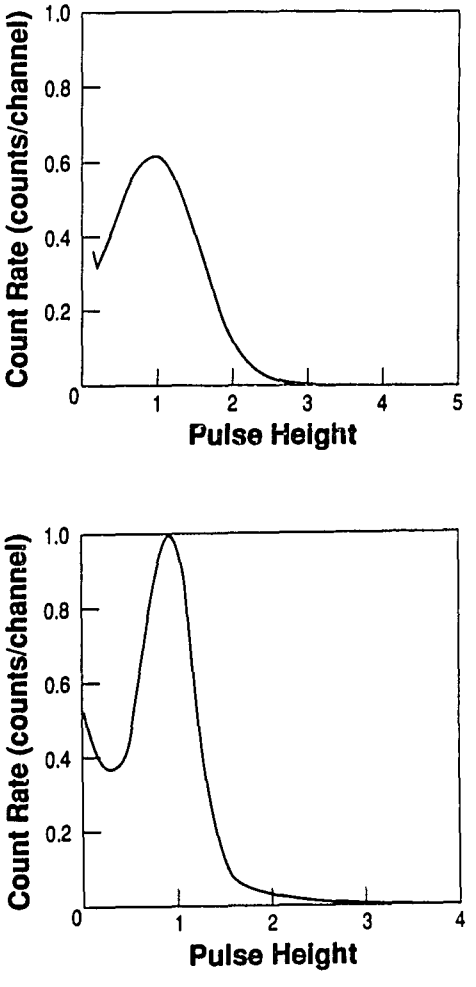

Fig. A.2 Pulse height distribution curves for 943-02 and 1333 PMTs.

intensity are measured, well matched PMTs should be used. There are very wide variations in response within a given tube type.

When using any PMT the tube should not be subjected to wide variations in light intensity, and after prolonged darkness a warm-up time was found to be necessary (about one hour of comparable illumination when making exacting measurements). Also, the temperature of the tube should be kept constant because the spectral response of the photocathode, and the dark count rate, is temperature dependent. The cooler should not be run at maximum capacity. The actual temperature of the tube in that case is generally the external coolant water minus some fixed cooling capacity.

APPENDIX B

HIGH NUMERICAL APPERTURE ATTACHMENT FOR HELIUM DEWAR

A reoccuring problem in investigating the optical behavior of materials at low temperatures is the inability to use small spot sizes because of typical dewar designs. This is particularly true when using liquid helium dewars. In order to obtain the close working distances necessary to employ relatively high power objectives (obviated to some extent by the use of reflective objectives) a special attachment was made (fabricated by Charles Burkhart of the Optical Scieces Center Machine Shop) for use with the Air Products (now APD Cryogenics) LT3-110 dewer. The device is composed of three parts (figure B.1): a cold finger, a cold shield, and a vacuum shroud. The solid angle that the cold finger sees of ambient radiation is about the same as that of the stock design, although the thermal path to the liquid helium source point is substantially larger. By observing the shift of the band edge of several material samples (GaAs MQW and quantum dot samples) it appears the cold finger sample location is about 10K to 15K. If it is desired to absolutley minimize spot size the aberrations due to the windows will, of course, have to be dealt with. This includes a slight negative power due to the concavity of the windows, brought about by the internal vacuum. In this case a smaller windowed design might be in order.

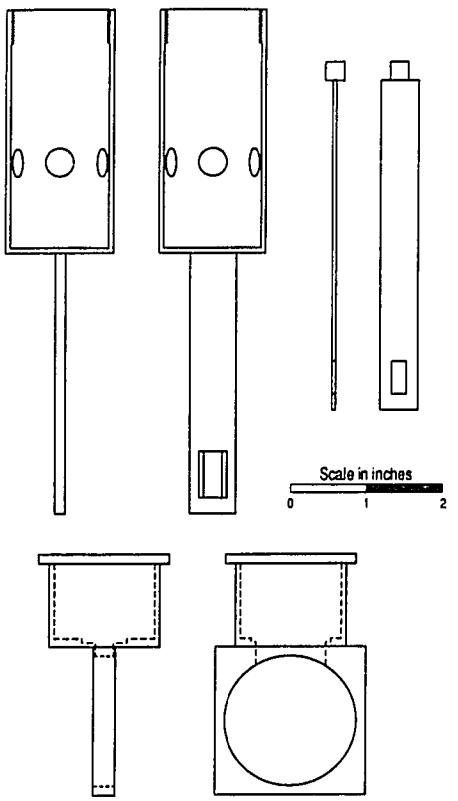

Fig. B.1 Special high N.A. attachment for APD Cryogenics He dewar LT3-110.

APPENDIX C

LAMP STABILIZATION CIRCUIT

When measuring extreamly small percentage signals, system stability is critical. When doing spectroscopy, along with several other devices, it is essential to have a very stable light source. In the quantum confined Franz-Keldysh measurement the noise associated with the Xenon lamp, normally used for other measurements, was completely unacceptable. Although some of this noise was due to arc filament wander, which can be treated by the use of a magnetic field, power supply noise was at the root of the problem. Other light sources with 'low noise' power supplies were tried, but to no avail. The following simple circuit, figure C.1 , produced an exceptional stability of .001% when employed with a standard 12V filament bulb and three high capacity, deep cycle automotive batteries. The draw back is that the light bulb does not supply very high irradiance, but gains may be made by the judicious choice of a specialty bulb (tungsten halogen as an example).

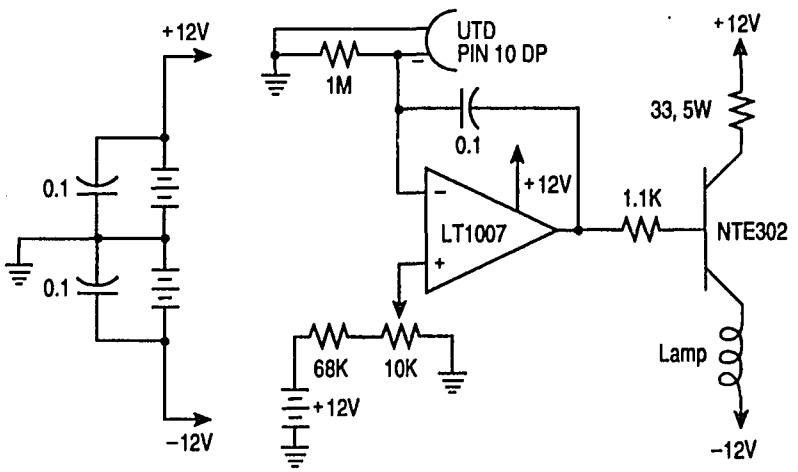

Fig. C.1 Circuit for stabilization of a 12V filament lamp.

REFERENCES

Abu-Mustafa, Y.S., and Psaltis, D., Sci. Am. 256(3) 88 (1987)

Anderson, D. and Erie, M.C., Opt. Eng. 26 434 (1987)

Ashcroft, N.W. and Mermin, N.D.,*Solid State Physics*, Holt Rinehart and Winston, Philidelphia, PA (1976)

Brus, L.E., J. Chem. Phys., 80(9) 4405 (1984)

Chadi, D.J., Walter, J.P., Cohen, M.L., Petroff, Y., and Balkanski, M., Phys. Rev. B5 3058 (1972)

Chemla, D.S., and Miller, D.A.B., J. Opt. Soc. Am. B2 1155 (1985)

Cohen, M.L., Proc. 7th Int. Conf. II-VI Semiconducting Compounds, W.A. Benjamin Inc., New York (1967)

Ekimov, A.I., Efros, Al.L., and Onushchenko, A.A., Solid State Comm. 56 (11) 921 (1985)

Esch, V., Chavez-Pirson, A., Liu, L.C., Risbud, S., Khitrova, G., Koch, S., Gibbs, H.M., Conference on Lasers and Electro-Optics (CLEO), Baltimore MD, THNN5 (1989)

Gibbs, H.M., *Optical Bistability: Controlling Light with Light*, Academic Press, New York (1985)

Georgekutty, T.G. and H.-K. Liu Appl. Opt. 26 372 (1987)

Hache, F., Ricard, D., and Flytzanis, C., Appl. Phys. Lett. 55 1504 (1989)

Hong, J. and Psaltis, D., Opt. Lett. 11 812 (1986)

Hopfield, J.J., Proc. Natl. Acad. Sci. USA 79 2554 (1982)

Kohonen, T., *Self-Organization and Associative Memory*, Springer-Verlag, New York, 1984

Lee, Y.H., Chavez-Pirson, A., Rhee, B.K., Gibbs, H.M., Gossard, A.C., and Wiegmann, W., Appl. Phys. Lett. 49 1505 (1986)

Lifshitz, I.M. and Slezov, V.V., J. Phys. Chem. Solids 19, 35 (1961)

Madelung, O., Shulz, M., and Weiss, H. eds., Landolt-Bornstein, Vol. 22, Springer-Verlag, Berlin (1987)

Miller, D.A.B., Chemla, D.S., Damen, T.C., Gossard, A.C., Wiegmann, W., Wood, T.H., and Burrus, C.A., Appl. Phys. Lett. 45 13 (1984)

Miller, D.A.B., Chemla, D.S., Damen, T.C., Gossard, A.C., Wiegmann, W., Wood, T.H., and Burrus, C.A., Phys Rev B32 1043 (1985)

Miller, D.A.B., Chemla, D.S., and Schmitt-Rink, S., Appl. Phys. Lett. 52,2154 (1988)

Owechko, Y., Dunning, G.J., Marom, E., and Soffer, B.H., Appl. Opt. 26 1900 (1987)

Paek, E.G. and Psaltis, D., Opt. Eng. 26 428 (1987)

Potter, B.G. and Simmons, J.H., Phys. Rev. B37(18) 838 (1988)

Psaltis, D. and Farhat, N., Opt. Lett. 10 98 (1985)

Shiff, L.I., *Quantum Mechanics*, McGraw-Hill Book Company, New York (1955)

Wang, L., Esch, V., Feinleib, R., Zhang, L., Jin, R., Chou, H.M., Sprague, R. W., Macleod, H.A., Khitrova, G., Gibbs, H.M., Wagner, K., and Psaltis, D., Appl. Opt. 27 1715 (1988)

Wang, Y., Herron, N., Mahler, W., and Suna, A, J. Opt. Soc. Am. B 6(4) 808 (1989)

Weiner, J.S., Chemla, D.S., Miller, D.A.B., Wood, T.H., Sivco, D., and Cho, A.Y., Appl. Phys. Lett. 46(7) 619 (1985)